Journal of Hydrology 648 (2025) 132468

Contents lists available at ScienceDirect

Journal of Hydrology

journal homepage: www.elsevier.com/locate/jhydrol

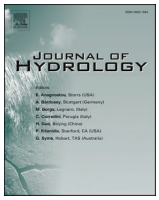

Research papers

A simplified method for estimating the alpha coefficient in surface velocity based river discharge measurements

Dario Pumo *, Francesco Alongi, Carmelo Nasello, Leonardo V. Noto

Dipartimento di Ingegneria – Università degli studi di Palermo, Viale delle Scienze, Ed. 8, 90128 Palermo, Italy

ARTICLE INFO

This manuscript was handled by D. Han, Editor-in-Chief, with the assistance of Pierfranco Costabile, Associate Editor

Keywords:
River discharge
Flow velocity measurement
ADCP
Velocity-area method
Vertical velocity profile
Surface velocity
Particle image velocimetry

ABSTRACT

Remote sensing techniques for river monitoring facilitate faster measurement campaigns compared to traditional methods, reduce risks to personnel and instruments, and allow measurements under critical flow conditions. An alpha coefficient (α) is commonly employed to convert surface velocities, obtained by contactless techniques, into depth-averaged velocities, which are used for the application of the velocity-area method for assessing discharge. Some optical-based software programs use a constant α value, based on a theoretical "standard". However, analyses of empirical vertical velocity profiles in real cases reveal that α can significantly deviate from this standard due to various factors (roughness, turbulence, etc.).

This study analyzes several ADCP (Acoustic Doppler Current Profiler)-based measurements in Sicily, Italy, to explore factors influencing flow velocity distribution and potential errors from using the standard α for discharge estimation via surface velocity-based methods. The results confirmed substantial variability in α, which is functionally related to some geometric factors characterizing the cross-section shape and the specific vertical where the velocity profile is computed. The generated dataset of empirical α values is also used to implement an Artificial Neural Network (ANN), offering a straightforward tool suitable for non-contact techniques. The ANN predicts α at any vertical of a measurement transect as a function of variables however necessary for discharge assessment by non-intrusive methods, leading to depth-averaged velocity estimates from surface velocities that are more accurate than those derived from conventional approaches, as demonstrated by four test cases.

1. Introduction

River monitoring is crucial for environmental, societal, and economic sectors. Accurate monitoring facilitates early detection of potential flooding events, enabling timely warnings. It is also essential for an effective water resources management, supporting decisions regarding water allocation for agricultural, industrial, and civil uses. Furthermore, rivers serve as sensitive indicators of climate change; their monitoring offers valuable insights into climate impacts on water levels, flow rates, and seasonal patterns, informing adaptation strategies (Arnell and Gosling, 2013). Reliable discharge data are also routinely used for the design and maintenance of hydraulic infrastructures, and support scientific research in hydrology, ecology and, more in general, in environmental sciences, providing essential information for models' calibration.

Discharge measurements in river sections are traditionally performed using the velocity-area method (Herschy, 1998; Le Coz et al., 2008; Le Coz et al., 2012; Despax et al., 2016; Harding et al., 2020). This involves measuring velocities along several verticals of the cross-section to estimate each sector's discharge contribution, with the total discharge determined by integrating these contributions. Current meters (mechanical or electromagnetic) are conventionally used to implement this method discretely (Herschy, 1998). The introduction of Acoustic Doppler Current Profilers (ADCPs) marked a technological advancement, enabling the application of the velocity-area method in a continuous form. However, ADCPs have well-known limitations (Díaz Lozada et al., 2023); for instance, they require sufficient water levels to discretize the water column into an adequate number of cells, depending on the sensor type. Riverbed roughness and vegetation can make bottom velocity measurements unreliable due to the side lobe effects, while surface measurements are limited by the acoustic sensor's submersion depth.

Traditional techniques using current meters and ADCPs are costly, time consuming, and intrusive. Direct contact with water poses risks to

* Corresponding author.
E-mail addresses: dario.pumo@unipa.it (D. Pumo), francesco.alongi01@unipa.it (F. Alongi), carmelo.nasello@unipa.it (C. Nasello), leonardo.noto@unipa.it (L.V. Noto).

https://doi.org/10.1016/j.jhydrol.2024.132468
Received 2 August 2024; Received in revised form 7 November 2024; Accepted 13 November 2024
Available online 1 December 2024

operator safety and instruments integrity, especially under hazardous conditions like floods. Some limiting environmental and hydraulic conditions may necessitate significant deviation from standards measurement protocols (i.e., ISO 748:2021), leading to inaccurate estimations (Pelletier, 1988; Díaz Lozada et al., 2023).

An innovative approach gaining increasingly attention in river monitoring involves non-contact measurement methods, including radars, remote sensing and satellite imagery (Costa et al., 2000; Costa et al., 2006; Fulton and Ostrowski, 2008; Le Coz et al., 2010; Chen and Liu, 2020). Radar- and image-based techniques provide non-intrusive, reliable estimates of surface velocity fields by remotely observing the motion of the water surface. Radar instruments utilize the Doppler effect to measure velocity. Handheld radar devices are portable and easily adaptable to the specific measurement conditions, while fixed radar gauges enable continuous monitoring (Alimenti et al., 2020). Image-based techniques, such as Large-Scale Particle Image Velocimetry, LS-PIV (Fujita et al., 1998; Muste et al., 2008), and Large-Scale Particle Tracking Velocimetry, LS-PTV (Li et al., 2013; Tauro et al., 2017), use commercially available and inexpensive recording devices. These methods acquire sequences of frames that are processed to track displacements and velocities of floating tracers, either naturally present or artificially introduced. Image processing is performed with specific software, often free and open-source (Le Coz et al., 2014; Thielicke and Stamhuis, 2014; Patalano et al., 2017; Perks, 2020; Ljubičić et al., 2024).

For these techniques, the velocity-area method for river discharge estimation requires simplifying assumptions to convert surface values into depth-averaged velocities. Some image-based analysis software, such as FUDAA-LSPIV (Le Coz et al., 2014), RIVeR (Patalano et al., 2017), and SSIMS-Flow (Ljubičić et al., 2024), include discharge calculation module that use a scaling coefficient to derive depth-averaged velocities. This coefficient (α), often called alpha or velocity coefficient (Biggs et al., 2021; Biggs et al., 2023), is defined as the ratio of depth-averaged to surface velocities along the same vertical. It can be applied either globally, as a single average value for the entire section under analysis, or locally for each cross-section vertical. The coefficient is frequently set to a standard "default" value (α*) of 0.857 (Costa et al., 2000; Le Coz et al., 2010; Hauet et al., 2018), which was obtained under the assumptions of a reference river roughness and a vertical velocity profile following a theoretical law (Rantz, 1982; Creutin et al., 2003; Costa et al., 2006; Hauet et al., 2008; Kim et al., 2008).

Empirical evidence (e.g., Welber et al., 2016) indicates substantial deviations of actual vertical velocity profiles from theoretical laws, leading to discrepancies in the coefficient α from α*. The spatial distribution of the velocity across a river cross-section is highly influenced by various geomorphological and hydraulic factors. Channel morphology significantly affects vertical velocity distribution; irregular cross-sectional shapes correlate with variability in velocity profiles (Bradbrook et al., 2000). Additionally, riverbed and banks roughness, influenced by structural characteristics and the possible presence of vegetation, contributes to the observed variability in vertical velocity profiles. Hydraulic flow conditions and turbulence also play crucial roles in shaping profiles. A notable deviation of the empirical profiles from monotonic theoretical laws is the so-called dip phenomenon, where peak velocity occurs below the water surface (Yang et al., 2004). The dip effect is linked to the section geometry, particularly the ratio of section width to water depth, and is more common in wide, shallow sections (Bahmanpouri et al., 2022a; Bahmanpouri et al., 2022b).

The so-called entropy-based approach (Chiu, 1989) offers an alternative option to estimate discharge from surface flow velocity, accounting for the presence of the dip phenomenon. The method has been refined by various authors (e.g., Moramarco et al., 2017; Koussis et al., 2022; Vyas et al., 2024). Moramarco et al. (2017) assumed that the entropy velocity profile at the vertical of maximum flow velocity applies to all verticals in a cross-sectional area. The approach involves two preliminary steps: (i) determining a site-specific entropy function, and (ii) estimating the dip, in terms of depth of maximum velocity below the surface and its value, as a function of the surface velocity, as proposed by Fulton and Ostrowski, (2008). The entropy function, which links mean flow velocity to the maximum velocity, is empirically derived by locally calibrating an entropic parameter based on observations of paired maximum and depth-averaged velocities. For the dip estimation, Moramarco et al. (2017) adapted a model by Yang et al. (2004), introducing a corrective factor to account for secondary currents, which is estimated through an iterative process. Vyas et al. (2024) proposed a refined version of this model, while Koussis et al. (2022) further extended the approach by applying the principle of maximum entropy to determine the most probable velocity distribution in the vertical, based on the observed surface velocities.

The entropy-based approach represents a very promising frontier, since it is currently the only method able to explicitly consider the dip phenomenon. Model's reliability strongly depends on calibration; the entropy function and the entropic parameter need to be locally calibrated at a given river site, requiring robust and large velocity dataset. This may limit the generalizability of this approach at rivers without site-specific data. However, some studies (e.g., Fulton et al., 2020; Vyas et al., 2020) suggest that the entropy function in a section may remain constant over time, regardless of hydraulic conditions, while Moramarco and Singh (2010) proposed a method suitable at ungauged sites for its derivation based on some geometric and hydraulic river cross-section characteristics.

The present study is specifically focused on the most used approach in practical applications, which is that based on the coefficient α. The work aims to: i) explore the variability of the coefficient across various field cases; ii) assess possible inaccuracy arising from using the standard α* in estimating depth-averaged velocities and discharges via non-contact techniques; iii) propose a novel and practical method for estimating vertical-specific α (local α_l), based on easily retrievable variables during field campaigns, such as the distance from riverbanks, water depths and cross-sectional shape indicators. To achieve these aims, the study set the following objectives: (1) analyze a large database of velocities derived from over 70 ADCP-based field measurements in different rivers of Sicily (Italy); (2) implement a standard procedure for empirically derive vertical velocity profiles from ADCP data; (3) estimate surface and depth-averaged velocities from these empirical profiles to derive empirical α_l at each vertical; (4) develop and test a data-driven soft-computing method using an Artificial Neural Network (ANN) to predict α_l in absence of ADCP data; (5) verify improvements in depth-averaged velocity and discharge estimation via non-contact techniques using the ANN compared to conventional approaches.

For the last objective, image sequences were acquired alongside with ADCP measurements at four test cases and processed with the LS-PIV method to derive empirical surface velocities across a given transect for each case. Different methodologies are then applied to determinate the corresponding depth-averaged velocity profile, including procedures based on: i) the standard α*; ii) a site specific global value of α, derived from extrapolated ADCP data using the Qrev software (Mueller, 2016); iii) local α_l values predicted by the ANN. The comparison between the resulting profiles across test cases, confirmed the importance of considering local alpha coefficients, variable along the cross-section, over a single, global coefficient, highlighting the ANN potential compared to conventional approaches.

The paper is structured as follows. Sect. 2 outlines theoretical background, field protocols and software, with detailed information provided in the Supplementary Material (SM). This section also describes the proposed procedure for deriving empirical vertical velocity profiles, surface velocities, and α_l from ADCP data. The ANN implementation methodology is outlined in Sect. 2, with details in the SM, which also reports the results of different sensitivity analyses. Sect. 3 presents the results, including the analysis of empirical α_l, the ANN performance, and the test conducted with LS-PIV data, while key implications are discussed in Sect. 4.

2. Materials and methods

2.1. Theoretical background

Predicting the variability of flow velocity across a river section is a complex task influenced by numerous factors. The spatial distribution of velocity is shaped by complex interactions among channel geometry and slope, vegetation, roughness, river morphology, obstructions, sediment load, and turbulence (Afzalimehr and Dey, 2009; Afzalimehr et al., 2019; Huai et al., 2019). To reconstruct flow velocity distribution across a river's wetted area, theoretical models for vertical velocity profiles are often used (Sect. S1, SM), such as the logarithmic velocity curve derived from the "law of the wall" (Petrie and Diplas, 2016). While the logarithmic law is widely accepted, empirical evidence shows that it properly represents only certain portions of a river, typically within the inner flow region. Real-world vertical profiles can deviate significantly from the logarithmic law; a notable phenomenon is the occurrence of peak velocity below the water surface, known as the "dip phenomenon", first reported more than a century ago (Francis, 1878) and observed also in laboratory experiments (Absi, 2011; Kundu and Ghoshal, 2012). When the dip occurs, the logarithmic law requires appropriate modifications for applicability (Sarma et al., 2000; Yang et al., 2004; Guo et al., 2005; Bonakdari et al., 2008; Lassabatere et al., 2013).

In practice, simple equations are often preferred over the logarithmic one. The power law (Eq. S2, SM) is a viable alternative, often used in the following simplified form:

$$u(z) = \beta \bullet z^{p} \tag{1}$$

where u is the flow velocity at height z, while β and p are locally calibrated parameters reflecting flow conditions, channel geometry, and roughness. Experimental data indicate p values ranging from 0.01 to 0.50 (Papadimitrakis and Orphanos, 2009; Lee et al., 2013), with higher values associated with rough and turbulent channels. However, observations in most natural rivers generally report narrower p ranges, from 0.14 to 0.17 (Le Coz et al., 2010; Welber et al., 2016; Johnson and Cowen, 2017; Biggs et al., 2023).

ADCP can capture complex flow patterns and help fit velocity distribution functions to vertical velocity profiles. However, due to the cost and limited availability of ADCPs, flow measurements are often taken at various depths using current meters along specific cross-sectional verticals. These spot measurements can be used to derive depth-averaged velocities, v_{dep}, based on assumptions about vertical velocity distribution, with accuracy improving with the number and spatial distribution of the acquired measurements. According to the standard ISO 748:2021 (Sect. S2, SM), various methods can derive v_{dep} depending on the number of sampled depths. When only surface velocity, u_s, is available (e.g., via radar- or image-based techniques), v_{dep} is calculated by scaling u_s with a dimensionless scaling factor, the velocity or alpha coefficient (α), defined as:

$$\alpha = \frac{v_{dep}}{u_s} \tag{2}$$

Sect. S2 (SM) presents different empirical and semi-empirical methods for estimating α, distinguishing between "global" α_g, i.e. a single value valid for the entire cross-section, and "local" α_l, specific to each vertical (Biggs et al., 2021). For simplicity, a global α* of 0.857 is often adopted as "standard" or "default" value; this derives from the integration of a power law velocity profile with standard exponent of 1/6, referring to the well-known Manning's formula (Rantz, 1982; Welber et al., 2016; Smart and Biggs, 2020). However, observational studies have shown that α* frequently fails to approximate empirical α values adequately (Welber et al., 2016). For instance, Turnipseed and Sauer (2010) reported α values ranging between 0.84 and 0.90, Hauet et al. (2018) found ranges from 0.70 to 0.90, while Johnson and Cowen (2017) noted values exceeding 1.10, due to irregular velocity profiles and wind effects, and low values (i.e., 0.39) in the presence of submerged vegetation. Based on previous studies, the guideline by Biggs et al. (2021) suggests α values based on site roughness and locally calibrated power-law exponents: around 0.86, for "normal" roughness and p between 0.14 and 0.17; low values (minimum 0.67), for rough sites with high p (0.25 to 0.50); up to 0.91 for smooth site with low p (e.g., 0.01); extreme values (e.g., 0.6 or 1.2) only in exceptional cases.

Accurate α estimation is crucial for minimizing errors in discharge estimation using non-contact techniques. The adoption of α* is common in many LS-PIV based software (e.g., FUDAA-LSPIV, RIVeR, SSIMS-Flow), but often introduces significant uncertainty. Wind can cause important disturbances, influencing α values and causing substantial deviations from α*; therefore, discharge measurements based on surface velocities methods should be avoided when wind effects are visible on the water surface.

When ADCP measurements are available, a site-specific alpha (α_{Qrev}), can be derived from extrapolated ADCP data using the Qrev software, developed by the United States Geological Survey (Mueller, 2016). This program performs linear interpolations for missing data through dedicated modules. A normalized vertical velocity profile representative of the entire section is obtained by fitting a power law (Legleiter and Kinzel, 2021), using as exponent a default value ($p = 1/6$), an automatically computed fitting value, or a user-defined value. Various options (Sect. S3, SM) are available for extrapolating the velocity profile to portions of the water column typically unsampled by the ADCP (e.g., top and bottom). With default settings, including the default exponent, and the "Power" options for both "Bottom" and "Top" extrapolation methods, α_{Qrev} results in the standard α*. For testing purposes, both α* and α_{Qrev} will be considered in this study, with the latter obtained by considering locally calibrated exponents and setting "No Slip" and "Power" options as extrapolation methods at the "Bottom" and "Top", respectively. Additional information is provided in Sect. S3 (SM), and detailed Qrev user-manuals provide further guidance (Mueller, 2016).

2.2. Field campaign

2.2.1. ADCP based measurements

A large field campaign was carried out between 2020 and 2024 at different rivers in Sicily (Italy), including channels of various types and sizes, under different hydraulic regimes. The rivers (Fig. 1) are predominantly natural and characterized by irregular geometries with riverbed and banks material like rock, sand, or gravel, and presence of vegetation. The *Platani river* (PL) is the only artificial river, with concrete riverbed and banks, and a regular trapezoidal geometry.

A total of 70 independent measurements were carried out using an ADCP at the 13 different rivers reported in Fig. 1 and Table 1, with multiple measurements over time (i.e., from 2 to 9 per river). Each individual measurement is identified by an alphanumerical identification code (*ID*) reported in Table 1, with the first two characters referring to the river under evaluation (Fig. 1) followed by a number referring to the progressive chronological order of measurement in that river. Table 1 also provides the main results obtained from ADCP in terms of cross-sectional average velocity (V_{avg}) and total discharge (Q).

An overview of the main geometric and hydraulic characteristics explored across the full set of measurements is reported in Fig. 2, in the form of empirical cumulative distribution functions (cdf), $F(x)$. Discharge measurements were conducted in rivers with width (W) ranging from around 4 m up to 24 m, and maximum water depth (h_{max}) ranging from 0.30 m to 2.40 m. The measured values of Q spanned from 0.02 m^3/s to 7.22 m^3/s, with V_{avg} from 0.01 m/s to 0.93 m/s.

Simultaneous measurements using the LS-PIV technique were also conducted in four test cases, highlighted in bold in Table 1, to assess empirical surface velocity profiles along the transects where ADCP benchmark measurements were available. The adopted workflow and experimental setup are fully described in Sect. S4 (SM) and summarized in Table 2, while only the main aspects are reported here. An area of

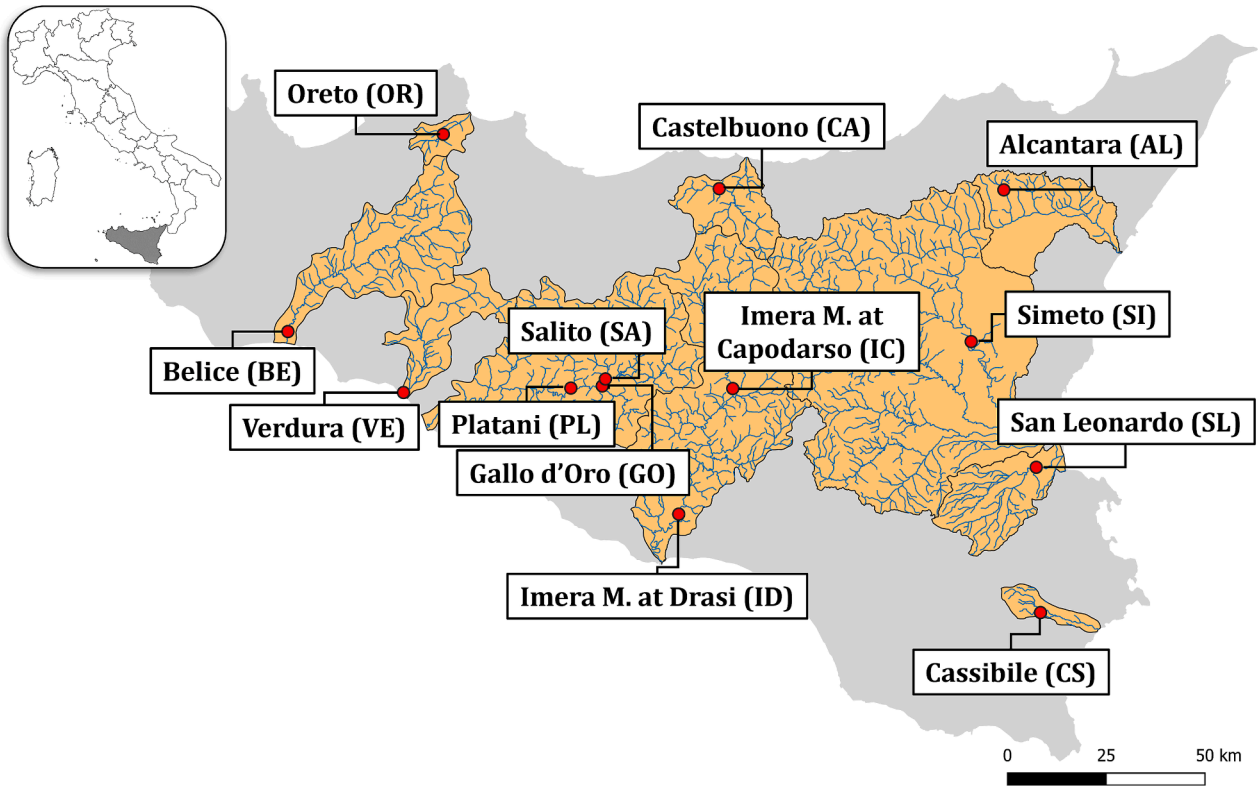

Fig. 1. Study area: Sicily (Italy), highlighted in grey also in the inset plot. Monitored rivers (river name and assigned ID) and location of discharge measurement sections (red markers). The watershed (yellow areas contoured by black lines) and river network (blue lines) are also highlighted for each monitored river. (For interpretation of the references to colour in this figure legend, the reader is referred to the web version of this article.)

interest, containing the cross sectional transect sampled by the ADCP, was identified for each case, placing some clearly visible markers, used as Ground Control Points (GCPs), with coordinates retrieved from topographic surveys by a differential GPS. Tracer wooden material was introduced manually on the water surface, following some criteria defined in Pumo et al. (2021) to ensure an adequate tracer density and spatial distribution. Long video sequences (i.e., longer than 3 min in all cases) were acquired by a digital camera either mounted on a tripod or using a drone. Except for the case with the highest cross sectional average velocity (i.e. VE8), the operative frame-rate was halved with respect to the acquisition frame-rate (i.e., passing from 25 and 30 fps to 12.5 and 15 fps, respectively) to minimize the risk for possible occurrence of sub-pixel displacements of tracer between consecutive frames (Pumo et al., 2021). The procedure defined in Alongi et al. (2023) was then used for automatically detecting and extract an optimal portion from each original sequence based on the frame-by-frame analysis of the tracer density and distribution.

The obtained sub-sequences were processed using the SSIMS-Flow (Ljubičić et al., 2024), which is an open-source image velocimetry software based on the Gunnar Farneback's algorithm (Farnebäck, 2003). The software was here preferred to other common software (e.g. PIVLab, FUDAA-LSPIV, etc.) since it is rather versatile and complete, giving the opportunity to manage the pre-processing, frames analysis, and post-processing phases within a unique software. The software is briefly described in Sect. S4 (SM); more details can be found in Ljubičić et al. (2024).

2.3. Procedure for estimating empirical alpha coefficients from ADCP data

The first objective of this work was to develop a specific procedure for evaluating empirical local α_l from ADCP data. The selected criteria were designed to establish a rigorous methodology for obtaining consistent and robust estimations of α_l across different verticals from various field measurements, which are subsequently aggregated into a single sample for comprehensive analysis. The procedure proposed includes the following steps, detailed in the next paragraphs: i) discretization of the wetted area into cells, organized in vertical sectors to form a regular grid; ii) derivation of vertical velocity profiles at the central axis of each sector, which is assumed to represent the entire sector; iii) estimation of the local α_l. Some settings for this procedure were based on a sensitivity analysis, with results provided in the SM (Figs. S1 and S2).

Field measurements were conducted using a StreamPro ADCP by Teledyne RD Instruments, which collects both velocity and bathymetry data. During data acquisition along a vertical, the StreamPro ADCP divides the water column into equal-sized bins (either 5 or 10 cm), and collects an ensemble of velocities at each bin. ADCP measurements are characterized by some regions where the instrument is unable to collect velocities: (i) a "top blanking distance," which includes the transducer immersion depth (typically set at 5 cm) and the region immediately below the transducer face (~3 cm); (ii) a "bottom blanking zone" adjacent to the riverbed, affected by the side-lobe effect for about the 6 % of the vertical depth.

Each field measurement was processed by the WinRiver II software and conducted according to the protocol described in Sect. S5 (SM), adhering to the operational standards and guidelines provided by the USGS (Mueller et al., 2009) and the World Meteorological Organization (WMO, 2008). Discharge assessment from field measurements is derived from the analysis of multiple reciprocal acquisitions (Measurement Transects, MTs) along the same river cross-section. During the entire field campaign, a total of 594 MTs were acquired, with, on average, eight MTs per measurement (Fig. 2d) retained after excluding inconsistent MTs, based on the Dynamic Residual Analysis (DRA) by the WinRiver II.

Table 1
Field measurements with Identification Code (*ID*), time of acquisition (*DATE*, in the format *dd.mm.yyyy*), cross-sectional average velocity (V_{avg}) and total discharge (Q). Cases where LS-PIV measurements were also conducted are highlighted in bold.

ID		DATE	V_{avg} (m/s)	Q (m^3/s)	ID		DATE	V_{avg} (m/s)	Q (m^3/s)	ID		DATE	V_{avg} (m/s)	Q (m^3/s)	ID		DATE	V_{avg} (m/s)	Q (m^3/s)
BE	1	01.07.2020	0.20	0.82	CS	1	29.07.2020	0.072	0.38	ID	1	12.02.2020	0.10	2.09	OR	1	07.02.2020	0.08	0.30
	2	*08.06.2021*	0.19	0.70		2	*23.09.2020*	0.077	0.42		2	*17.06.2020*	0.02	0.34		2	*02.07.2020*	0.05	0.16
	3	*18.10.2021*	0.18	0.65		3	*21.05.2021*	0.065	0.35		3	*15.09.2020*	0.05	0.95		**3**	***14.09.2020***	**0.05**	**0.16**
	4	*11.03.2022*	0.30	1.49		4	*15.06.2021*	0.064	0.33		4	*06.05.2021*	0.07	1.34		4	*01.04.2021*	0.24	0.72
	5	*01.04.2022*	0.39	2.44		5	*06.09.2021*	0.073	0.31		5	*08.11.2021*	0.05	0.93		5	*04.06.2021*	0.08	0.22
	6	*28.04.2022*	0.24	1.07		6	*09.11.2021*	0.10	0.48		6	*07.04.2022*	0.11	1.83		6	*15.10.2021*	0.21	0.78
	7	*20.05.2022*	0.25	1.07		7	*09.06.2022*	0.068	0.32		7	*10.05.2022*	0.37	7.22		7	*06.06.2023*	0.38	1.89
CA	1	*15.01.2020*	0.04	0.18	*IC*	1	*11.02.2020*	0.084	1.07	*PL*	1	*18.06.2020*	0.15	0.23	*VE*	1	*29.01.2020*	0.47	1.66
	2	*10.06.2020*	0.01	0.05		2	*17.06.2020*	0.012	0.10		**2**	***08.09.2020***	**0.19**	**0.32**		2	*11.03.2022*	0.46	1.11
	3	*09.04.2021*	0.10	0.27		3	*15.09.2020*	0.038	0.38		3	*13.04.2021*	0.27	0.69		3	*01.04.2022*	0.93	3.87
	4	*04.06.2021*	0.01	0.02		4	*06.05.2021*	0.077	0.81		**4**	***07.05.2021***	**0.20**	**0.63**		4	*28.04.2022*	0.23	0.72
	5	*23.11.2021*	0.14	0.39		5	*08.11.2021*	0.018	0.31		5	*08.02.2022*	0.37	2.54		5	*12.04.2023*	0.54	1.55
	6	*15.06.2022*	0.12	0.50		6	*24.04.2022*	0.044	0.86		6	*08.04.2022*	0.18	1.12		6	*20.09.2023*	0.08	0.08
SL	1	*21.04.2023*	0.05	0.82	*AL*	1	*24.06.2020*	0.047	0.14		7	*17.05.2023*	0.41	2.74		7	*13.11.2023*	0.43	1.04
	2	*26.10.2023*	0.01	0.11		2	*14.05.2021*	0.038	0.30		8	*12.12.2023*	0.12	0.33		**8**	***12.01.2024***	**0.75**	**2.31**
SI						3	*16.06.2021*	0.034	0.08	*GO*						9	*12.01.2024*	0.89	3.61
	1	*20.04.2023*	0.12	2.45		4	*11.11.2021*	0.138	0.37		1	*07.06.2023*	0.135	1.05	*SA*	1	*07.06.2023*	*0.138*	0.683
	2	*26.10.2023*	0.06	0.57		5	*06.05.2022*	0.111	0.29		2	*12.12.2023*	0.008	0.06		2	*12.12.2023*	0.01	0.03

2.3.1. Grid discretization of the wetted-area

The wetted area obtained from each ADCP bathymetric survey, was discretized into a grid using a standard procedure for all cases. This process involves an initial division of the cross section into vertical sectors and a successive horizontal division of each sector into cells.

The top river width at the measurement cross-section is binned in equal-width vertical sectors with step-size δ_{SW}, starting from a central sector whose middle axis aligns with the central axis of the entire section. Sectors adjacent to the riverbanks that are narrower than δ_{SW} are merged with neighboring sectors to create wider sectors. The value of δ_{SW} was set equal to 40 cm, based on the sensitivity analysis (Fig. S1) that also evaluated alternatives of 20 cm and 60 cm. This configuration resulted in an average of 22 sectors per measurement, with a minimum of 11 sectors in the narrowest cases. The chosen δ_{SW} ensures a sufficient number of sectors per cross-section to effectively characterize the potential variability of α along the transect and, at the same time, it provides a high percentage of adequately sampled sectors by the ADCP, resulting in fewer sectors being discarded due to insufficient sample size compared to the other alternatives. The appropriateness of this choice is further supported by the resulting variability of α_l, which was comparable to results obtained with a larger δ_{SW}, characterized by broader coverage of ADCP sampled points.

Each sector is further divided vertically, starting from the water surface, forming columns of equally sized cells. A cell-depth of 10 cm, i.e. the maximum possible ADCP bin-size, is used for sectors with a total water depth of at least 60 cm. For shallower sectors, considering the further reduction of the sampled depth due to the top and bottom blanking zones, a cell-depth equal to the ADCP bin-size (either 5 or 10 cm) is used, thus preserving the original acquisition resolution. Adopting an approach analogous to that used for the cross-section discretization in sectors, when the depth of the bottom cell adjacent to the riverbed is less than the designated cell-depth for the sector, it is merged with the upper cell. This criterion optimizes the available ADCP data for each sector, ensuring the maximum number of sectors with at least three well-sampled cells, assumed here as the minimum required to derive empirical vertical velocity profiles. This also justifies the choice of using possibly cell-depth of 5 cm in verticals with water depth less than 60 cm, as using a 10 cm cell-depth would often result in fewer than three cells per sector.

Following this procedure, each measurement's wetted area is divided into a regular grid of rectangular cells (Fig. 3a), predominantly 40 cm wide and 10 cm high. Exceptions occur in regions frequently undersampled by the ADCP, such as: i) shallow sectors, where a finer cell discretization (i.e., 5 cm instead of 10 cm) is used if possible; ii) near riverbanks, where cells might be wider (up to 79 cm); iii) near the riverbed, where cells could be deeper than the those above, with depth ranging from 5 cm to 19 cm.

2.3.2. Empirical vertical velocity profiles and local alpha coefficients

The WinRiver II data extraction module is used to retrieve the ensemble of velocities collected by ADCP at each bin (ADCP-ensemble) from each MT along with the corresponding bin-center position. For each measurement grid, ADCP-ensembles with bin-centers within a grid cell from various MTs are aggregated to form a unique "cell-ensemble" of velocities associated with the grid-cell center, as illustrated in Fig. 3b.

The cell-ensembles of each sector are extracted and analyzed to reconstruct a sector-specific vertical velocity profile. An example is shown in Fig. 3c, where ADCP velocities for each cell are depicted as grey points, and each cell-ensemble is also visualized as blue boxplot. Outliers (red '+' points in Fig. 3c), identified as velocities exceeding ± 1.5•IQR (IQR = interquartile range), are excluded from the analysis. Similarly to the Qrev approach, the retained velocities within a cell are averaged to determinate the final velocity associated with the cell-center (i.e., ensemble-averaged cell velocity, $v_{avg,c}$). The sample-size and the coefficient of variation (*CV*) for each cell-ensemble are also recorded. Values of $v_{avg,c}$ based on fewer than a threshold number of samples (δ_{SZ} =

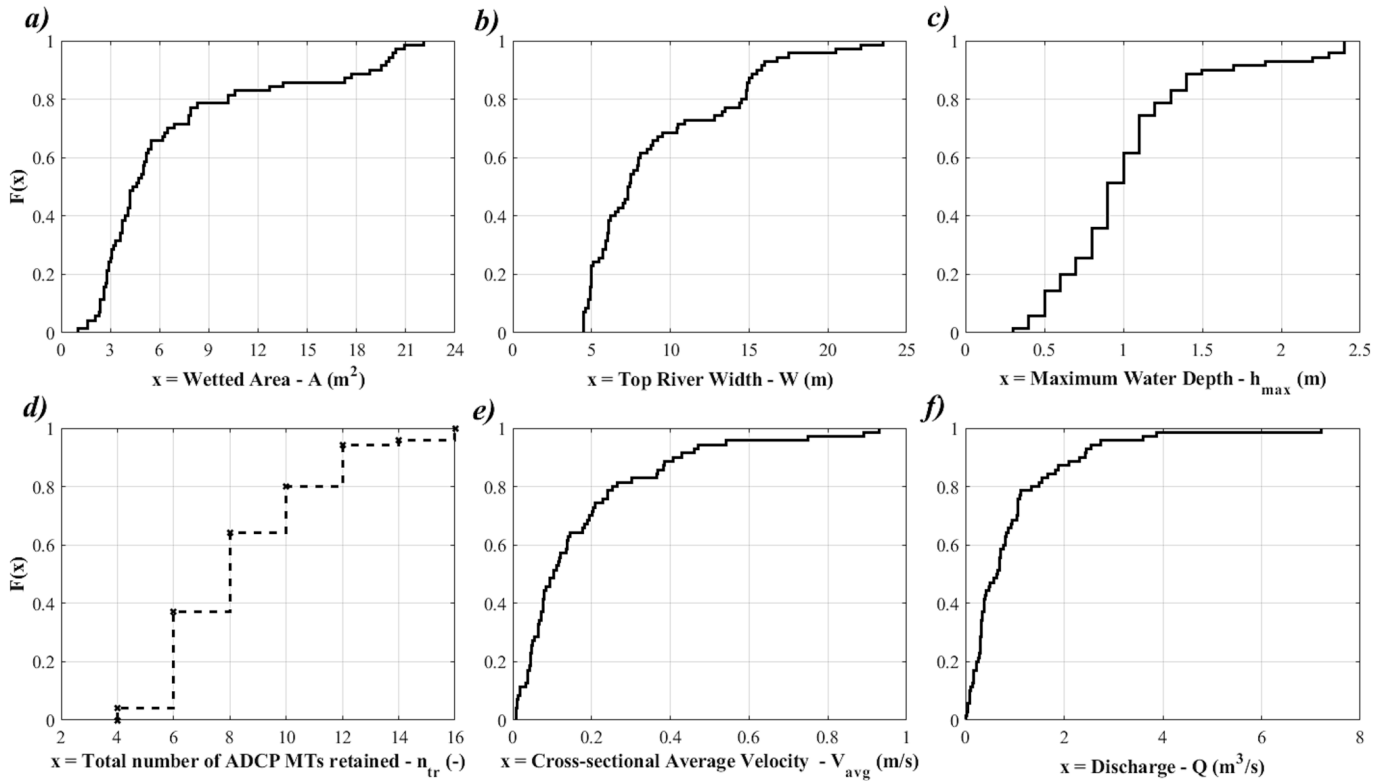

Fig. 2. Empirical cdf, $F(x)$, of the wetted area (A), top river width (W), maximum water depth (h_{max}), number of ADCP MTs retained per each measurement (n_{tr}), cross-sectional average velocity (V_{avg}), and discharge (Q), considering all measurements listed in Table 1.

Table 2
Experimental setup for LS-PIV measurements: *ID* and *DATE* (corresponding to Table 1), acquisition mode, operative frame-rate (fps), spatial resolution (px/m), total number of GCPs.

ID		*DATE*	Acquisition mode	frame-rate (fps)	Resolution (px/m)	Number of GCPs
OR	3	*14.09.2020*	fixed camera	12.5	104	4
PL	**2**	*08.09.2020*	drone	15	85	6
PL	**4**	*07.05.2021*	drone	15	100	8
VE	**8**	*12.01.2024*	drone	30	90	6

20) are discarded due to insufficient sample size (green markers in Fig. 3c). The threshold δ_{SZ} was chosen between 10 and 30 based on sensitivity analysis (Fig. S1, SM), balancing robustness and homogeneity in velocity estimations across profiles in different sectors and case studies; in particular, for δ_{SW} of at least 40 cm, $\delta_{SZ} = 20$ ensured variability of α_l comparable to using a more restrictive threshold (i.e., $\delta_{SZ} = 30$) while maintaining a high number of reconstructed profiles.

An empirical profile is derived for sectors with three or more retained $v_{avg,c}$ (red vertical markers in Fig. 3c), representing over 50 % of total cells in that sector; otherwise, the sector is discarded to ensure adequate representation of vertical velocity variability. A discrete empirical vertical velocity profile over the depth well-sampled by the ADCP, is created using retained $v_{avg,c}$ and assuming linear variation between consecutive cell centers (stepwise solid magenta line in Fig. 3c). A power law is then fitted on retained $v_{avg,c}$ values, assuming null velocity at the riverbed (i.e., no-slip condition) to account for the riverbed friction effects. A weighted interpolation is performed, with weights inversely proportional to the cell-ensemble CV, under the hypothesis that low dispersion of the ADCP-ensemble indicates robust $v_{avg,c}$ measurements. The least squares method, with constraint on the exponent ranging from 0.01 to 0.50 (Papadimitrakis and Orphanos, 2009; Lee et al., 2013; Johnson and Cowen, 2017), is used for fitting.

The goodness-of-fit is assessed using the coefficient of determination (R^2) and the Willmott index, δ (Willmott et al., 2012, Sect. S7, SM), a statistical performance index scarcely sensitive to errors concentrated in outliers, varying from 0 to 1 (perfect matching). A threshold for δ (δ_w) was subsequentially applied to differentiate between cases where the observed profiles strictly adhere to a power law (PL profiles, $\delta \geq \delta_w$) and those where this assumption does not hold (No Power Law profiles, NPL, $\delta < \delta_w$). The value of δ_w was set at 0.65 based on sensitivity analysis (Fig. S2, SM), after exploring a range from 0.50 to 0.75, and it marks a value where the variability of alpha for PL profiles stabilizes, while maximizing the number of PL profiles. Using this threshold, the R^2 of the power laws in all PL profiles resulted higher than 0.90, confirming the reliability of the adopted metric and threshold.

For both PL and NPL cases, the power law is used to extrapolate the profile to the riverbed, including the bottom blanking zone. The upper part of the profiles (from the shallowest cell-center with retained $v_{avg,c}$ to the water surface, including the upper blanking distance) is reconstructed using the fitted power law in extrapolation for PL profiles, while, for NPL profiles, a constant velocity equal to the shallowest retained $v_{avg,c}$ is assumed.

The surface velocity and the depth-averaged velocity are extracted from each empirical profile, and the empirical α_l is computed through Eq. (2). Additional data for each sector are also retrieved for the successive analysis, such as water depth at the sector central axis, distance from the nearest riverbank, top river width, average and maximum water depths of the cross-sectional area including the sector.

Using these criteria, empirical profiles were reconstructed in approximately 80 % of the available sectors from the full set of field measurements, resulting in 1,165 profiles with corresponding α_l and, on average, 17 profiles per measurement. A total of 342 profiles (29 %) were classified as PL profiles.

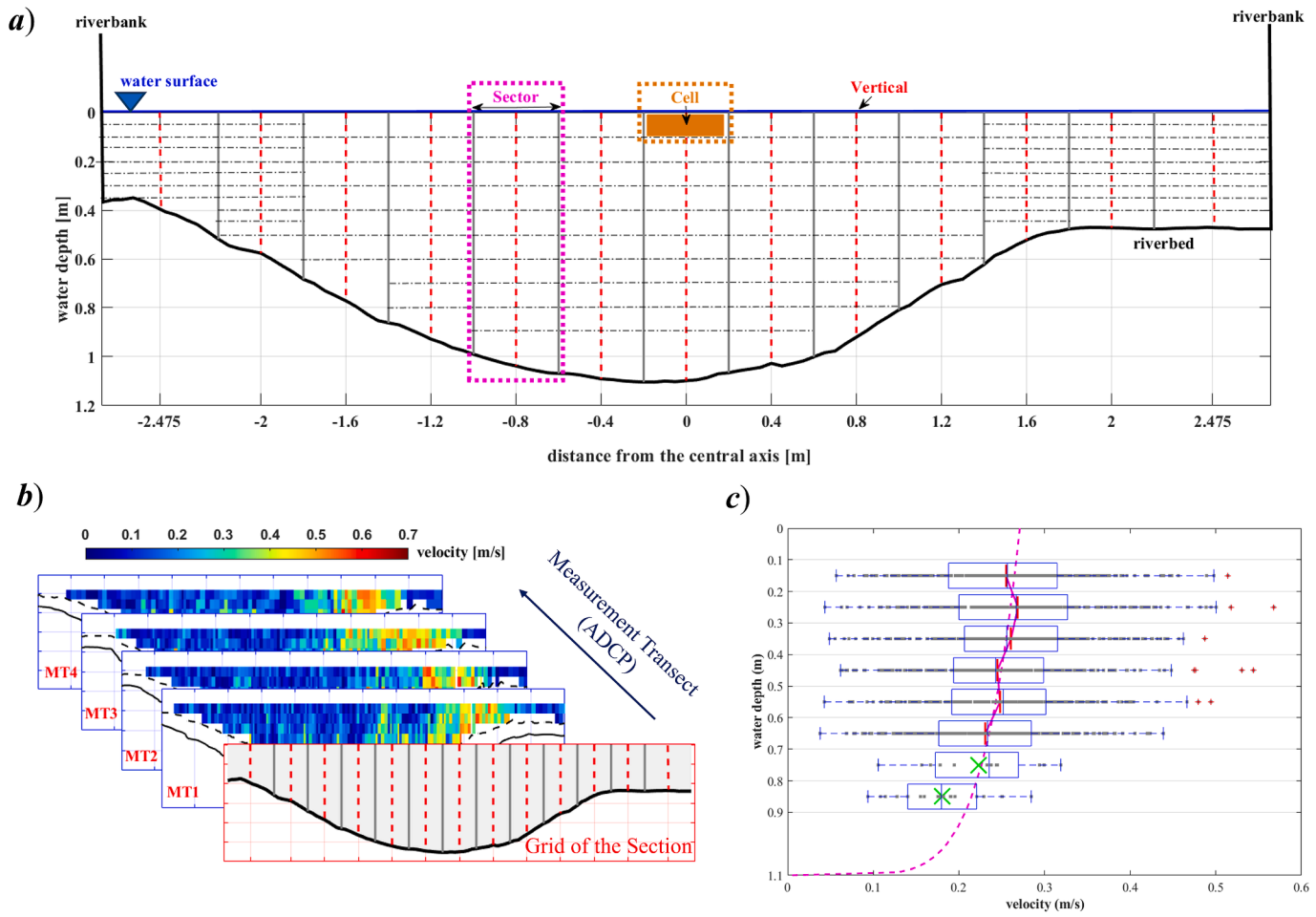

Fig. 3. Example of estimation of empirical vertical velocity profiles (case CA06 in Table 1). (*a*) Grid discretization of the wetted area, with sectors (vertical grey lines, see magenta box) and verticals (red dashed lines). Each sector is divided into cells (see orange box). Cells vary in size in shallow sectors (i.e. water depth lower than 60 cm) and/or near the riverbanks. (b) Velocity reconstruction by overlapping the section grid (red layer) with the different ADCP measurement transects, MTs (blue layers). Average bin velocities in each MT are shown in colormap. (c) Vertical velocity profile for the central sector. Cells are delimited by the horizontal grey grid. Grey points are individual ADCP measures within a cell, reported to the cell-center, and blue boxplots show cell-ensemble velocities. Red vertical markers indicate retained ensemble-averaged velocities, while green markers denote discarded values due to insufficient sample-size. The magenta dashed line represents the power law fit, assuming no-slip condition at the bottom. (For interpretation of the references to colour in this figure legend, the reader is referred to the web version of this article.)

2.4. Creation of an ANN for estimating local alpha coefficients

This study proposes a practical tool for improve the estimation of local alpha coefficients, α_l, compared to the standard α^*. The practical advantages of this tool include its reliance solely on information that are typically required for discharge estimation through radar or optical techniques. For this reason, differently from other approaches (e.g. Welber et al., 2016), this work focuses exclusively on easily measurable geometric variables as potential regressors of α_l. The proposed approach is based on the premise that using a single global α_g for the entire cross-section is often inappropriate because it does not account for variability in α along the section. Factors such as the roughness could significantly influence α, and some simply derivable variables, like the distance from riverbanks and water depth at specific verticals in relation to the wetted area shape, can indicate roughness effects on α in that vertical and partially explain its variability.

A preliminary analysis of α_l values here derived from ADCP data was conducted to verify potential correlations with influencing factors, leading to the development of a modelling framework based on a feed-forward Multi-Layer Perceptron Artificial Neural Network (MLP-ANN) by the Neural Network Toolbox of MATLAB®.

The choice of a data-driven soft-computing model was deemed appropriate for the following reasons: i) a large dataset of empirical α_l values were available; ii) the dataset may contain uncertainty typical of ADCP measurements and those arising from the procedure used to compute empirical α_l; iii) the preliminary dataset analysis indicated a strongly nonlinear relationship between α_l and some explored factors; iv) data-driven models require no prior assumptions about the relationships between predictors and explained variables, and are often capable to recognize functional patterns, mitigating effects of noise and uncertainty in the data.

For a given vertical of a river cross-section with a known wetted area, the ANN provides a unique "output", that is the predicted α_l. A supervised learning algorithm was used for training, using a selection of the available empirical α_l as "target" response variables. The dataset for the ANN implementation (ANN-dataset) was created aggregating empirical α_l from all measurements, considering only values from PL profiles to exclude those potentially affected by local turbulence, dip phenomena or other factors that might cause consistent divergences from any theoretical profiles. The ANN uses variables indicative of the vertical under evaluation and the cross-section geometry as input data. Specifically, the predicted α_l is computed as a function of the water depth at the given vertical (h), the distance of the same vertical from the nearest bank (d), and two dimensionless ratios representative of the cross-

section shape: the maximum-to-average depth ratio (R_h) and the width-to-max depth ratio (R_{wh}), defined as follows:

$$R_h = \frac{h_{max}}{h_{avg}} \tag{3}$$

$$R_{wh} = \frac{W}{h_{max}} \tag{4}$$

where h_{avg} and h_{max} are the average and maximum water depths across the cross-section, respectively, and W is the top river width. The ratio R_h is always equal to or greater than one, approaching unity for rectangular cross-sections, while higher values occur in triangular cross-sections. The index R_{wh} is positive, with low values for narrow, deep sections and higher values for shallow, wide rivers. The ANN-dataset comprises 342 paired input–output samples, with each sample including an input set of four variables (h, d, R_h, R_{wh}) and the associated target output, α_l.

Alternative configurations of input parameters were previously investigated, by progressively adding and combining various factors influencing α_l, including those ultimately selected and others such as the cross-sectional wetted area (A), the wetted perimeter (P), the hydraulic radius (R), which combines A and P, and the same W, h_{avg} and h_{max} considered individually rather than in combined form such as in Eqs. (3) and (4). The final configuration was selected based on the best-performing ANN, measured by R^2 over simulated-empirical α_l values.

Some default settings for the development of MLP-ANNs in MATLAB were utilized, employing hyper-tangent activation functions for Hidden Layers (HLs) and a linear activation function for the Output Layer. Bias terms were included in each layer, and the weights and biases were initialized randomly. The ANN was created following a two-step trial-and-error procedure like that adopted in Pumo and Noto (2023). A single HL was used to maintain a simple topology, however exploring various degrees of complexity by varying the number of nodes in the HL (from 5 to 100) and testing a total of 96 different structures. The final ANN was selected as the best converging models (i.e. associated with the lowest Mean Square Error) across several (hundreds) training trials for each structure, as detailed in Sect. S6 (SM).

3. Results

3.1. Observed variability of the empirical alpha coefficients

A preliminary investigation of all 1,165 empirical α_l values was conducted to analyse the observed variability at each measurement of Table 1. Fig. 4a presents the average α_l (black line) and the range of variation (grey shaded area) for each measurement, also reporting α^* (orange line) for comparison. The measurements are ordered from left to right based on h_{max}, progressing from the shallowest to the deepest cross-section. Fig. 4b shows h_{max} and W, while Fig. 4c displays the total number of reconstructed empirical profiles (n_s) per measurement, with the darkest bars indicating the number of PL profiles. The observed range of α_l, from 0.63 to 1.50, was consistent with other studies (e.g. Welber et al., 2016). The average α_l per measurement ranged from 0.76 to 1.33, with a very high average value of 0.97 and an average variability range per measurement of 0.38. The data indicated that in about 83 % of cases, the average α_l exceeded α^*, with a noticeable increasing trend with h_{max}. Specifically, the average α_l was below α^* in most cases with h_{max} below 0.55 m, and in only in 2 out of 29 cases where h_{max} exceeded 1 m. Compared to the shallowest sections, those with high h_{max}, that are generally also wider, showed a higher number of reconstructed empirical profiles, and conversely, they presented a lower fraction of these adhering to a power low (Fig. 4c), confirming the importance of the section geometry in shaping the profiles.

Fig. 5 presents the results of the analysis on the entire aggregated sample of α_l (i.e., full-dataset) and its subset used to generate the ANN (i.e. ANN-dataset), exploring the variability of the coefficient with respect to the water depth (h) and the distance (d) from the nearest bank. The full-dataset was divided into three classes for h (Fig. 5a) and d (Fig. 5b),

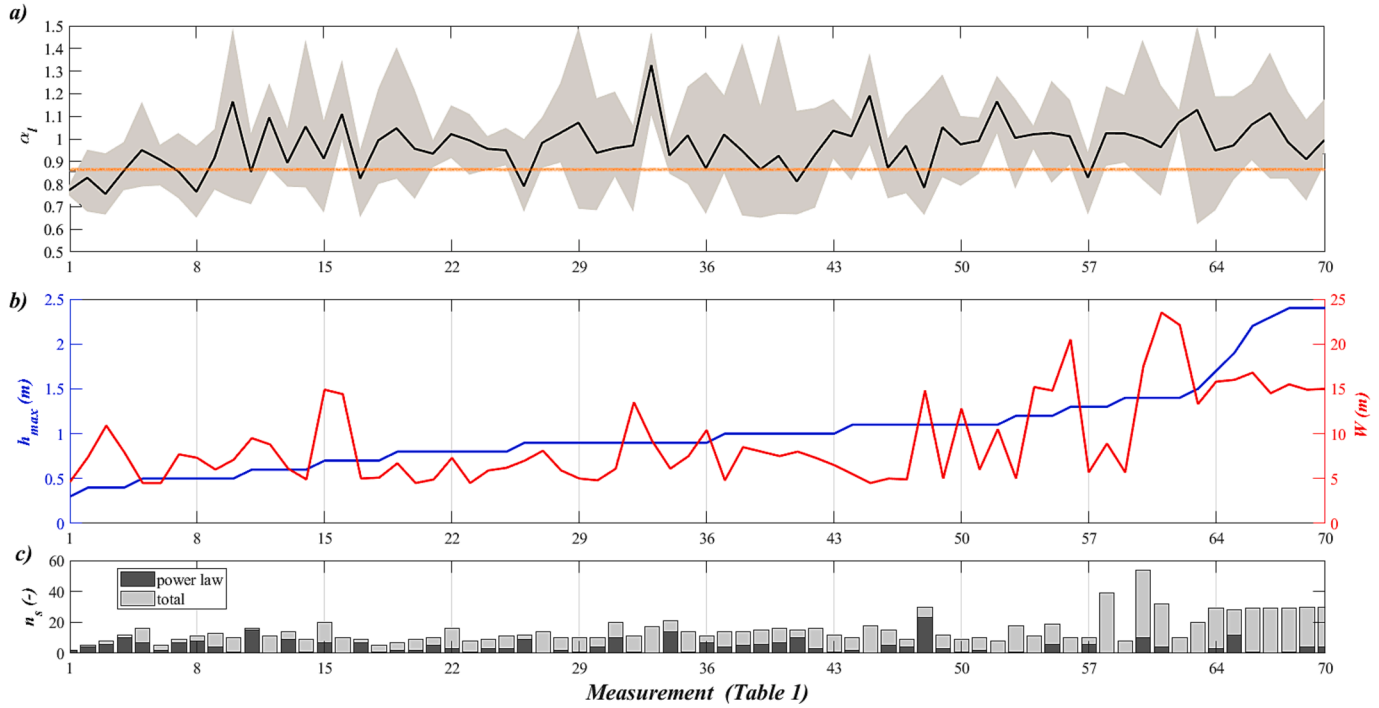

Fig. 4. Variability of the empirical α_l per measurement: (*a*) average value (black line) and variability range (grey shadow area) of α_l resulting at all measurements of Table 1; the orange line refers to the standard α^*; (*b*) maximum water depth, h_{max} (left y-axis, in blue), and top river width, W (right y-axis, in red), characterizing the cross-section for each measurement; (*c*) number of retained sectors per measurement, n_s, denoting the number of α_l computed per each measurement, with indication of the number of PL profiles. Measurements in all plots are ordered according to h_{max}, from the case with lowest value (on the left) to that with the highest one (on the right). (For interpretation of the references to colour in this figure legend, the reader is referred to the web version of this article.)

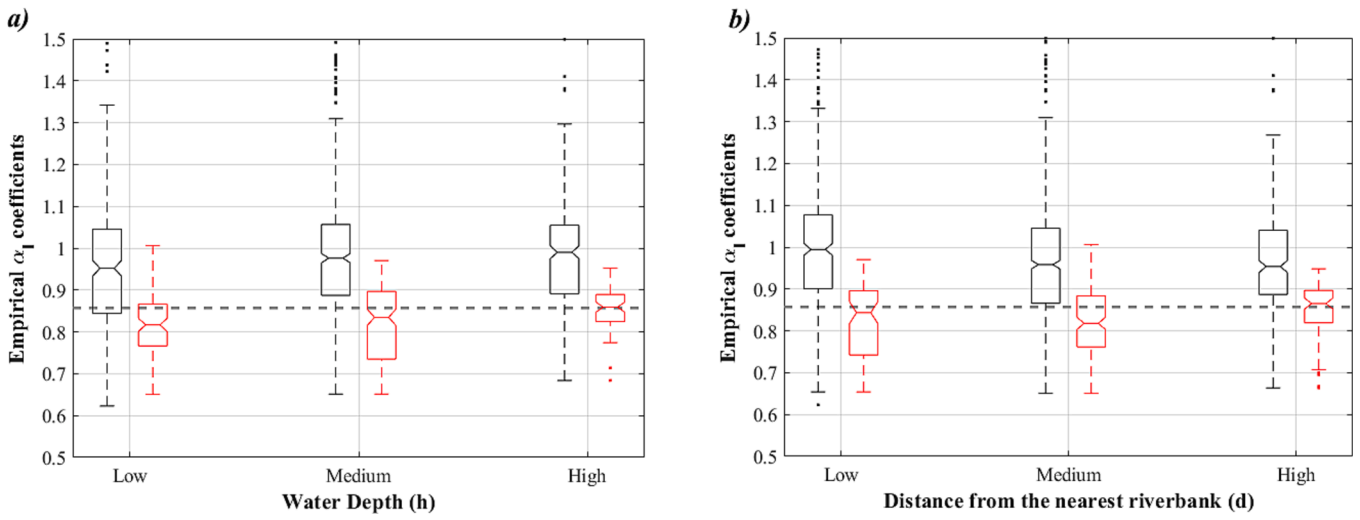

Fig. 5. Boxplots of the empirical α_l for different classes of (*a*) water depth, *h*, and (*b*) distance of the vertical from the nearest riverbank, *d*. *Low* ($h < 0.67$ m), *Medium* ($0.67 \leq h \leq 1.24$ m) and *High* ($h > 1.24$ m) classes for *h*, as well as *Low* ($d < 1.6$ m), *Medium* ($1.6 \leq d \leq 4.05$ m) and *High* ($d > 4.05$ m) classes for *d*, were defined based on the first and third quartile over the full-dataset. Black and red boxplots refer to the full-dataset and the ANN-dataset, respectively. Grey dashed lines refer to the standard α*. (For interpretation of the references to colour in this figure legend, the reader is referred to the web version of this article.)

using the first quartile (Q_1, 0.67 m for *h* and 1.60 m for *d*) and the third quartile (Q_3, 1.24 m for *h* and 4.05 m for *d*) as thresholds to define "*Low*" ($<Q_1$), "*High*" ($>Q_3$) and "*Medium*" (remaining values) classes. The ANN-dataset was classified using the same method and thresholds. The variability of α_l within each class is depicted in the form of boxplots, with the full-dataset represented in black and the ANN-dataset in red. The standard α* (dashed grey line) is reported in both plots for comparison. In both datasets, the *Low* class shows the highest occurrence of α_l associated with verticals in shallow rivers and/or near riverbanks, where roughness effects are potentially more pronounced. Conversely, the *High* class includes α_l from verticals generally less affected by roughness effects induced by riverbed and banks compared to the *Low* class.

Fig. 5 shows that α* serves as a reasonable estimate of α_l only for verticals following a PL profile, forming the ANN-dataset, as indicated by the red boxplots, where median values predominantly align with the α* line. Conversely, most empirical α_l values derived from NPL profiles, which represent the majority of the full-dataset (black boxplots), cluster around values significantly higher than α*. Fig. 5a and b illustrate the influence of *h* and *d* on α_l, respectively. Empirical α_l generally increases with both *h* and *d*, and, for both variables, the *High* class exhibits reduced variability in α_l compared to the *Low* and *Medium* classes. This effect is much more pronounced for PL cases than for NPL cases. In the full-dataset, empirical data reveal a different trend with respect to *d* (black boxplots in Fig. 5b), where the median α_l values decrease from the *Low* to the *High* class, with similar interquartile ranges across all classes.

This analysis, particularly focusing on the *High* classes for both variables and datasets, reveals that verticals with reduced roughness effects (i.e., with high *h* and *d*) are characterized by α_l values predominantly higher than α*. For other classes, multiple disturbance factors may

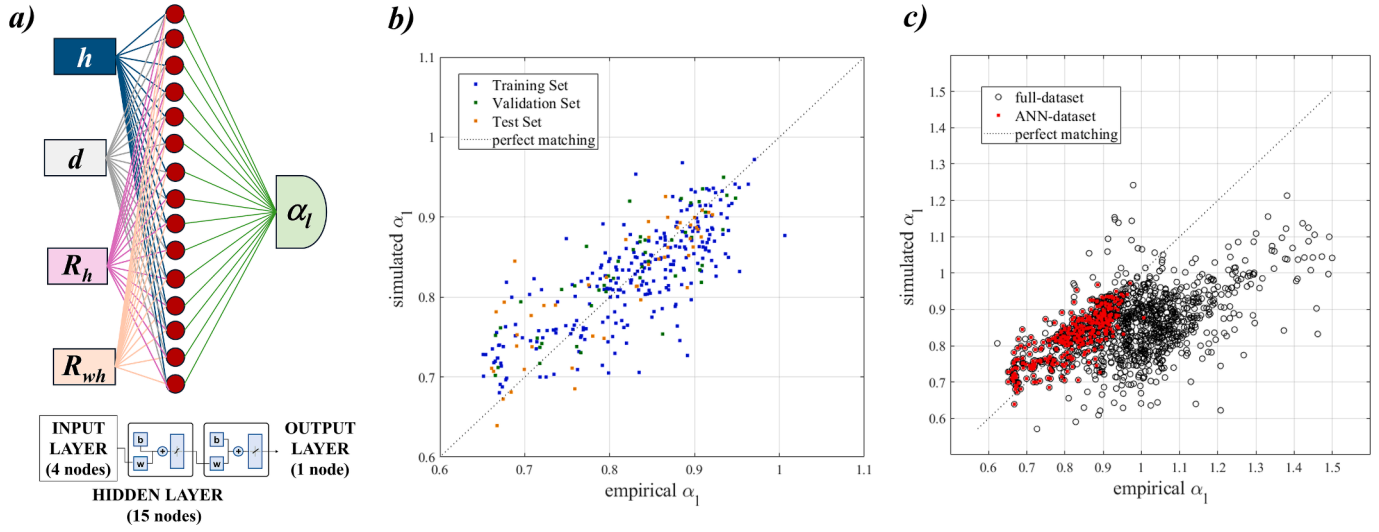

Fig. 6. (*a*) schematic representation of the ANN formed by an Input Layer with 4 nodes (*h*, *d*, R_h and R_{wh}), a Hidden Layer with 15 nodes and an Output Layer with a node (α_l). Hyper-tangent and linear activation functions have been used for the Hidden and Output layer, respectively, considering bias terms (*b*) at each layer (*w* in the bottom scheme refers the weights). (*b*) Regression plots of empirical vs. simulated α_l for the Training Set (blue markers), Validation Set (green markers) and Test Set (orange markers). (*c*) Regression plots for the full-dataset (black markers, 1,165 values) and the ANN-dataset (red markers, 342 values). Dashed grey line in the regression plots shows the 45° perfect matching line. (For interpretation of the references to colour in this figure legend, the reader is referred to the web version of this article.)

simultaneously influence the results, leading to a less predictable behavior and higher variability in α_l. For these cases, observed α_l ranged around the standard value only when the vertical velocity distribution was demonstrated to follow a power law-like profile (red boxplots in Fig. 5).

3.2. Performances of the ANN

The two-step training procedure resulted in a final ANN with 15 nodes in the HL. A schematic representation of its structure is shown in Fig. 6a, while Fig. 6b displays the regression plot between simulated-empirical values of α_l. The ANN achieved an R^2 value of 0.80 for the entire ANN-dataset, with similar values obtained separately for the Training Set ($R^2 = 0.78$) formed by the 70 % of the ANN-dataset, the Validation Set ($R^2 = 0.84$) and the Test Set ($R^2 = 0.83$), containing both the 15 % of data. It is important to note that the data was randomly divided into Training, Validation, and Test sets, with the sole constraint of excluding from the Training Set all samples derived from the four test cases listed in Table 2.

The satisfactory performance of the ANN is further supported by other error metrics, such as the Root Mean Squared Error ($RMSE = 0.037$), the Mean Absolute Percentage Error ($MAPE = 4.7$ %), and the maximum Absolute Error ($AE_{max} = 0.16$). A Perturbation-based Sensitivity Analysis (PSA) was performed on the trained ANN to assess the influence of input features (h, d, R_h, and R_{wh}) on output predictions and determinate their relative importance. Specifically, the analysis applied a perturbation ratio, ε_k, ranging from −50 % to + 50 % to all samples in the Validation and Test sets, following the procedure outlined in Sect. S6 (SM). The results of the PSA, summarized in Fig. S3 (SM), show an overall limited sensitivity of the ANN to input variations, with small changes in input features causing not significant changes in the output. The symmetric response to both negative and positive perturbations suggest the absence of directional bias in the ANN. The PSA also identified R_h and R_{wh} as the most influential features on the ANN's output across the entire perturbation range, with R_h showing the highest sensitivity. Their sensitivity varied significantly across perturbation levels, indicating a non-linear response of the ANN to variations in these features. This highlights the need for precise measurement of R_h and R_{wh} in practical applications. In contrast, h and d exhibited lower sensitivity, with negligible fluctuations across the perturbation range, underscoring the robustness and stability of the ANN to changes in these features, which are less critical in terms of data quality and precision compared to R_h and R_{wh}.

The comparison between empirical and simulated α_l for the full-dataset, as shown in the regression plot in Fig. 6c, reveals that the ANN's performance declines significantly when vertical velocity profiles deviate from a power law, yielding $R^2 = 0.54$, $RMSE = 0.14$, $MAPE = 13.1$ %, and $AE_{max} = 0.63$. The figure also indicates that several NPL profiles, excluded from the ANN-dataset, tend to have empirical α_l values around or above unity. Although the ANN predicts some α_l values above α^*, generally underestimates them, since it was trained considering exclusively PL cases and it has learned a relationship between surface and depth-averaged velocity typically resulting from a monotonically increasing vertical velocity profile. Thus, the ANN, based on the design criteria adopted, can effectively estimate α_l for power law like profiles, capturing its variability induced by some roughness related effects. Conversely, for NPL profiles, the ANN often fails due to its inability to account for more complex factors influencing α_l that were not considered during its training. The presence of such factors often determinates scarcely predicable vertical profiles with depth-averaged velocities similar, or even higher, than the corresponding surface velocity, and, consequentially, α_l exceeding the unity. Nevertheless, the ANN produces errors slightly smaller than those associated with using α^* for NPL profiles, where errors for the full-dataset would be: $RMSE = 0.15$; $MAPE = 14.6$ %; $AE_{max} = 0.64$. In summary, without access to ADCP data and under uncertainty about whether a vertical velocity profile follows a power law, the ANN provide reliable estimates of α_l at verticals with regular and monotonically increasing vertical velocity distributions. For irregular or locally disturbed profiles, the ANN's estimates are only slightly better, or comparable to, those obtained using α^*.

Fig. 7 illustrates the variability in α_l simulated by the ANN for two synthetic cases with different shapes (Type A and B) and maximum water depths ($h_{max} = 0.4$ m and 1.2 m). Both shape-types are symmetric trapezoids, with the lower base measuring 4 m for Type A and 1 m for Type B. Lateral sides have external angle of 75° and 15° for Type A and B, respectively. The resulting wetted areas, ranging from 1.0 m^2 to 6.6 m^2, fall within the range of the explored real cases. The α_l values are visualized using a consistent colour bar across the four cases, as indicated in the figure, with violet-scale colours representing values above α^*. The ANN tends to assign higher α_l in the middle of the cross-section compared to regions near the banks. Both shape and water depth conditions significantly influence the estimation of α_l at the various verticals. For Type A cases (upper panels of Fig. 7), which have R_h (Eq. (3)) close to one, the variation imposed in the water depth resulted in a significantly change in R_{wh} (Eq. (4)), which passes from 10.5 to 3.9 as h_{max} increases. This resulted in low variability in simulated α_l under shallow water condition (left upper panel), with values constantly above α^*. Similar α_l values are found under deeper water condition (right upper panel) in the middle section, decreasing rapidly towards the banks to values below α^*.

For Type B cases (lower panels), R_h is significantly higher than for Type A cases, and it is approximately 1.7 for both shallow and deep water depths. Here, the same variation in the maximum water depth resulted in a less relevant change in R_{wh}, which passed from 9.9 under shallow condition (left bottom panel) to 8.3 under the deeper (right bottom panel), similar to the Type A case under shallow water condition. An opposite behaviour to Type A is observed, with more pronounced α_l gradients moving from the middle section to the banks under shallow water conditions (left bottom panel) than under deeper conditions (right bottom panel). Nevertheless, the ANN still predicts the highest α_l values (above α^*) in the middle section.

3.3. Application and comparison of different approaches on field cases

Three methods for estimating alpha coefficients were applied to the cases with LS-PIV measurements listed in Table 2 and not considered for training the ANN. Surface velocity fields, estimated using the SSIMS-Flow, enabled the estimation of empirical surface velocities in transects where ADCP measurements were available. These surface velocities were rescaled using alpha coefficients as scaling factor to determinate depth-averaged velocity profiles, which were finally compared with benchmark profiles obtained from ADCP data. The proposed ANN and two conventional methods were employed to determinate both local and global α. The ANN-based method (method: *ANN*) provides local coefficients $\alpha_{l,ANN}$, which vary along the transect as a function of h, d R_h and R_{wh}. For global α estimation, we considered the standard alpha α^* (method: *STAND*) and the site-specific alpha, α_{Qrev}, derived from Qrev (method: *Qrev*).

The results are summarized in Table 3, while Fig. 8 provides a graphical comparison of the depth-averaged velocity profiles for all test cases. The comparison for each test case is limited to the portion of the cross-sectional wetted area that was adequately sampled by the ADCP and covered by tracer during the LS-PIV seeding phase, excluding also regions adjacent to the banks, where optical-based velocity estimates are often affected by border effects (Dal Sasso et al., 2018; Pumo et al., 2021). As shown in Table 3, this portion, referred to as "actual area", on average covered 68.7 % of the total cross-sectional area, accounting for a comparison transect extension that is 63.5 % of the top river width, and contributing 91.2 % to the total discharge measured by the ADCP (reported in Table 1).

Errors in the estimation of the depth-averaged velocity, v_{dep}, by the

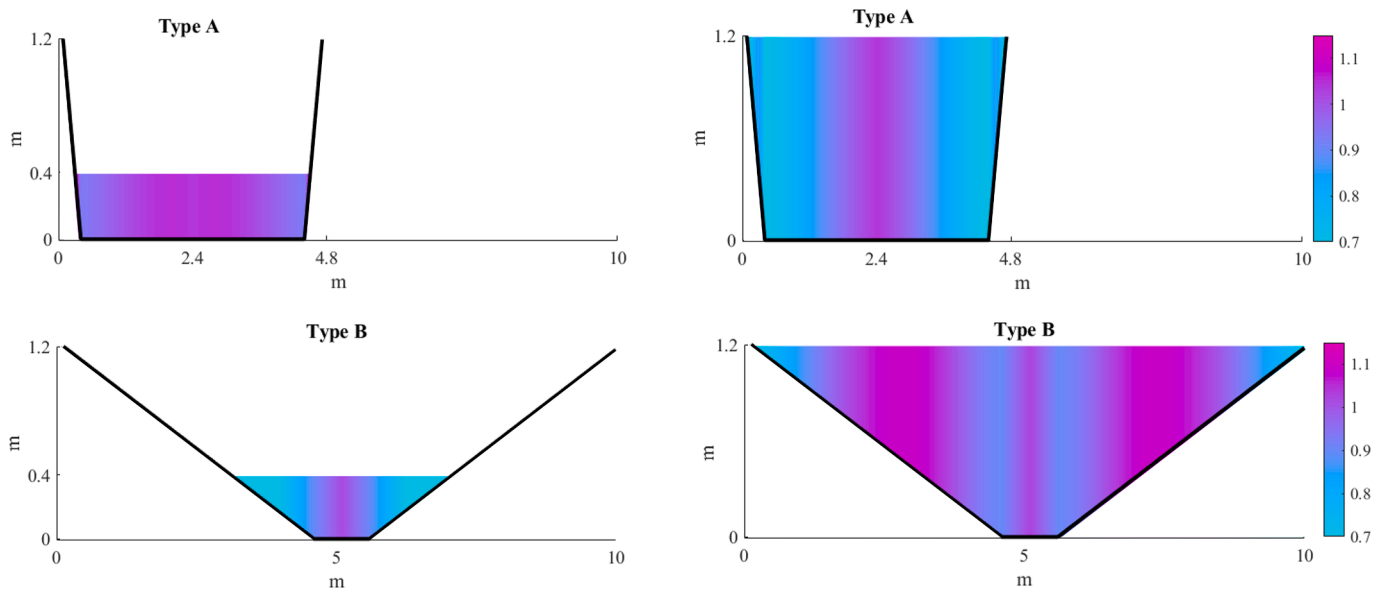

Fig. 7. Alpha coefficients (α_l) simulated by the ANN in two synthetic cases with different shape types (Type A, upper panels, and Type B, bottom panels) and under two different water depth conditions ($h_{max} = 0.40$ m in left panels, and $h_{max} = 1.20$ m in right panels). Sections have symmetric trapezoidal geometry, with lower base equal to 4 m and 1 m and lateral sides with external angle of inclination of 75° and 15° for Type A and B, respectively. The values of α_l are depicted according to the colorbar reported on the right (unique for all cases).

Table 3
Comparison of methods to convert surface velocities to depth-averaged velocities: i) *STAND*, using α*; ii) *Qrev*, using α_{Qrev}; and iii) *ANN*, using $\alpha_{l,ANN}$ from the ANN. The test case IDs are those used in Table 1. A^* and W^* are wetted area and top river width for the actual area considered for the comparison. $V^*_{avg,ADCP}$ and Q^*_{ADCP} are the benchmark cross-sectional average velocity and discharge from ADCP for the actual area. Percentages for A^*, W^* and Q^*_{ADCP}, indicate the actual area's contributions. Alpha coefficients used for each method are also reported, as well as the average, the min and max values (within brackets) of $\alpha_{l,ANN}$ for the *ANN*. $RMSE_{Vdep}$ refers to the errors between ADCP and surface-converted depth-averaged velocity (v_{dep}) computed at regular step of 0.1 m. Q^* and PE_{Q^*} are the discharge for the actual area and the Percentage Error obtained with each method, respectively. The lowest $RMSE_{Vdep}$ and PE_{Q^*} (best performances) for each case are highlighted in bold.

ID		A^*		W^*		$V^*_{avg,ADCP}$	Q^*_{ADCP}		method	alpha coefficients			RMSE (v_{dep})	Q^*	PE_{Q^*}
		(m^2)	(%)	(m)	(%)	(m/s)	(m^3/s)	(%)	acr.	(−)			(m/s)	(m^3/s)	(%)
OR	3	1.41	*65 %*	2.6	*60 %*	0.110	0.156	*95 %*	*STAND*	α*	0.857		0.032	0.180	*15.7 %*
									Qrev	α_{Qrev}	0.931		0.042	0.195	*25.6 %*
									ANN	$\alpha_{l,ANN}$	0.840	*(0.68–0.96)*	**0.020**	0.177	***13.4 %***
PL	**2**	1.16	*75 %*	2.8	*71 %*	0.224	0.261	*83 %*	*STAND*	α*	0.857		0.026	0.284	*8.6 %*
									Qrev	α_{Qrev}	0.972		0.055	0.321	*23.0 %*
									ANN	$\alpha_{l,ANN}$	0.818	*(0.79–0.87)*	**0.024**	0.271	***3.8 %***
PL	**4**	1.96	*65 %*	2.7	*61 %*	0.307	0.601	*95 %*	*STAND*	α*	0.857		0.037	0.626	***4.1 %***
									Qrev	α_{Qrev}	0.891		0.045	0.650	*8.1 %*
									ANN	$\alpha_{l,ANN}$	0.864	*(0.76–0.97)*	**0.033**	0.632	*5.1 %*
VE	**8**	1.79	*70 %*	3.3	*63 %*	1.186	2.122	*92 %*	*STAND*	α*	0.857		0.104	2.133	***0.5 %***
									Qrev	α_{Qrev}	0.812		0.117	2.016	*−5.0 %*
									ANN	$\alpha_{l,ANN}$	0.870	*(0.82–0.91)*	**0.082**	2.179	*2.7 %*

three methods compared to ADCP-based estimates, were evaluated at regular 0.1 m intervals along the comparison transect. The Root Mean Square Error ($RMSE_{Vdep}$) was then computed for each case (Table 3). The discharge contributions of the actual area (Q^*) resulting from the three methods were also computed and compared to the corresponding benchmark value from ADCP in terms of Percentage Error (PE_{Q^*}), as shown in Table 3.

The comparison of the alpha coefficients, reported in Table 3, shows α_{Qrev} values higher than α* for all cases expect VE8, which is that characterized by the highest flow velocity. In contrast, the ANN provided lower $\alpha_{l,ANN}$, with average values per measurement rather close to α* and a mean range of variation per measurement equal to 0.17. Analysis of the $RMSE_{Vdep}$ indicated that the *ANN* method outperformed the others, resulting in the lowest errors for all cases. Using $\alpha_{l,ANN}$ reduced, on average, the $RMSE_{Vdep}$ by 20 % compared to α* and 41 % compared to α_{Qrev}. Surprisingly, in none of the cases did the site-specific α_{Qrev} improve v_{dep} estimates compared to α*. This could be partially explained by the fact that α_{Qrev} was calculated using all ADCP data collected during a given measurement, including data from portions of the cross-sectional area excluded in determining the actual areas. These outcomes are also reflected in the estimation of discharge; the average PE_{Q^*} over the four test cases was lowest for the *ANN* method (6.3 %) compared to the *STAND* (7.2 %) and *Qrev* (12.9 %) methods. Regarding the estimated discharge Q^*, the *ANN* method performed best in OR3 and PL2, while it was approximatively equal to and worse than the *STAND* method in PL4 and VE8, respectively, yet still outperforming the *Qrev* method in all cases.

Fig. 8b help explaining why, despite having a lower $RMSE_{Vdep}$, the *ANN* method resulted in a less accurate estimation of Q^* at VE8 compared to the *STAND* method. The right part (i.e., for distances from the left bank over 2.2 m) of the v_{dep} profile obtained using α* (red line) underestimated the benchmark v_{dep} from ADCP (blue shaded area) more than the *ANN* method (black solid line). This underestimation compensated for the overall overestimation of v_{dep} in the left part of the

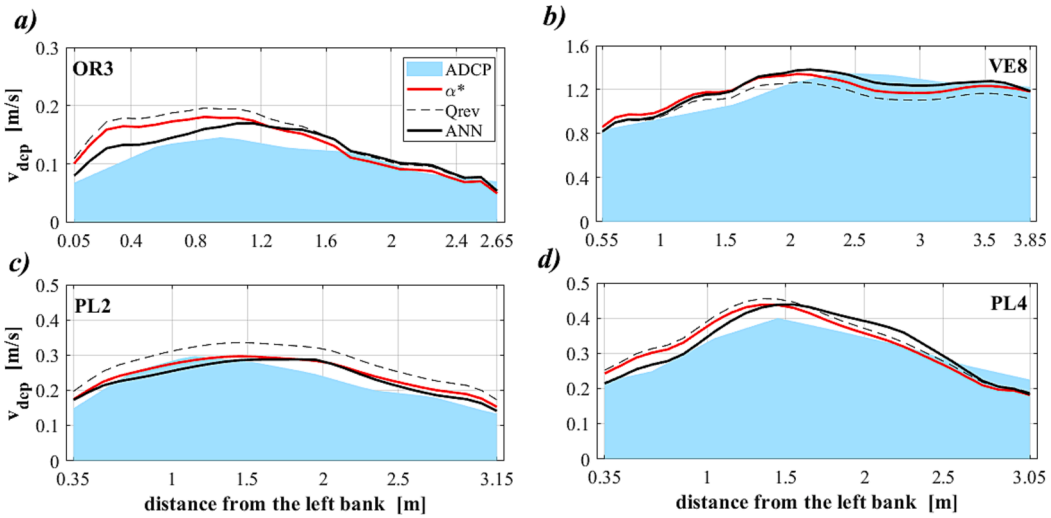

Fig. 8. Comparison between depth-averaged velocity (v_{dep}) profiles in the test cases: (*a*) OR3, (*b*) VE8, (*c*) PL2, and (*c*) PL4. ADCP-based benchmark profiles are reported as blue shaded areas. The profiles obtained from LS-PIV measurements applying the *STAND* (α*), *Qrev* (α_{Qrev}) and *ANN* methods are reported by red lines, dashed and solid black lines, respectively. (For interpretation of the references to colour in this figure legend, the reader is referred to the web version of this article.)

profile, which characterized all methods similarly and could be due to an overestimation of the surface velocity by the SSIMS-Flow. However, it is evident from all plots in Fig. 8 (and supported by the $RMSE_{Vdep}$ values in Table 3), that the distribution of v_{dep} along the transect obtained with the *ANN* method more closely matched that of the ADCP-based profiles, particularly near the banks. This is evident at case OR3 (Fig. 8a), where the left side of the ANN-based profile is shifted downward compared to the other methods and closer to the ADCP profile, due to the low local alpha values (lower than those obtained by the same ANN in the right side). This indicates that using variable alpha along the transect can represent possible differences between the shape of the surface velocity profile and that of the depth-average velocity profile better than using a global alpha coefficient (as in the *STAND* and *Qrev* methods), which only induces a scaling effect on the surface velocity profile.

The results in Table 3 also demonstrate that the accuracy of optical methods for discharge estimation primarily depends on the accuracy of the derived surface velocity profile; however, the estimation is significantly sensitive to the method adopted to convert surface velocities into depth-averaged values. For the examined cases, the maximum deviations between the different methods, expressed in terms of maximum percentage difference in the estimated Q^* with respect to the benchmark discharge value (i.e., $Q^*_{max} - Q^*_{min} / Q^*_{ADCP}$) ranged from 4 % (PL4) to 19 % (PL2), with an average value of 9.5 %, comparable with the accuracy of discharge estimations typically associated with the LS-PIV method (Fujita et al., 1998; Tauro et al., 2017; Alongi et al., 2023).

4. Discussion

Discharge measurements based on surface velocity often exhibits large uncertainty due to the assumptions required to convert surface velocity estimates into depth-averaged values, which are essential for the velocity-area method. This conversion typically relies on assuming or estimating the ratio of depth-averaged velocity to surface velocity (alpha coefficient, α), even if alternative approaches, such as those using the entropy theory (Moramarco et al., 2017), are gaining increasing attention.

The choice of α can significantly impact the measurement accuracy, as demonstrated in Sect. 3.3. Various methods can be used for estimating α, both practical and based on sound physical principles, with the choice depending on the specific site and the available information. A standard value, α*, in between 0.85 and 0.86 (Rantz, 1982) is often assumed as a global constant across the entire measurement transect, especially when site-specific information is lacking. This value, also used as default value in some LS-PIV software like FUDAA-LSPIV, originates from vertical velocity profiles that follow a 1/6th power law (Smart and Biggs, 2020). While α* applies under many flow conditions, α often varies significantly due to different and interacting factors (e.g. site geometry, flow conditions, wind effects on water's surface, riverbed and riverbank roughness, etc). Our analysis on a large dataset, including over a thousand of local alpha values (α_l) empirically derived via ADCP from several Sicilian rivers under different conditions, confirmed the variability of α, consistent with previous studies (e.g. Turnipseed and Sauer, 2010; Le Coz et al., 2012; Welber et al., 2016; Hauet et al., 2018; Alimenti et al., 2020). We observed α_l ranging from 0.62 to 1.50, with 80 % of values exceeding α*. However, when considering only empirical α_l at verticals with velocity profiles strictly following a power law (i.e. PL profiles: 29.4 % of the total), the standard value was exceeded only in 38 % of these cases; the mean (0.82) and median (0.83) of the α_l in PL profiles were rather close to α*.

Empirical local alpha values were functionally related to measurable variables characterizing the evaluation point along the transect (i.e. water depth, *h*, and distance from the nearest bank, *d*) and site's cross-sectional area (i.e. shape ratios R_h and R_{wh}, defined based on the top river width, and the mean and maximum water depth across the section). This relationship is partially explained by the different effects of roughness in shallower or bank-adjacent verticals, where higher variability and lower α_l values were observed in our dataset compared to verticals in the middle section and/or with high *h*. Welber et al., (2016) observed a similar behaviour, with empirical α_l derived for numerous field cases (36 measurements in 29 rivers in Israel, Italy and France) showing a significant influence of relative roughness (i.e. the ratio of median grain size to channel depth) and local water depth on alpha. In their study, α_l values larger than one were found in approximately a quarter of cases, while the lowest values were prevalently close to the banks; they concluded that the standard value is acceptable only for deep, hydrodynamically smooth channels where the assumption of a velocity profile following a theoretical law is well-supported by field conditions. Another study by Lee and Julien (2006) reported larger variability and lower α_l values (in the range 0.42–0.77) in a shallow gravel-bed river compared to a deeper, clay-bed canal, where the values ranged from 0.68 to 0.94.

To interpret the relationship between local alpha and the influencing factors *h*, *d*, R_h and R_{wh}, we generated an ANN exploiting the empirical dataset derived for the Sicily. The ANN, trained considering α_l from

verticals with verified power law-like profiles (PL profiles), accurately simulated the observed variability in α_l along the transect at verticals with monotonically increasing vertical velocity profiles. In contrast, discrepancies between empirical and ANN-simulated α_l values were significant, though still comparable to those using α^*, in verticals where the vertical profile deviated from theoretical laws (i.e., NPL profiles), indicating the potential influence of local factors complicating estimation with simple methods, such as the proposed ANN. However, as demonstrated in Sect. 3.3, using ANN-computed α_l values instead of a global alpha, either standard or site-specific, can significantly improve the characterization of alpha variability along a transect, consequentially enhancing discharge estimation accuracy with optical techniques. The advantages of using local alpha values are also reported in different field guidelines, such as those by Biggs et al. (2021), discussing various approaches for estimating site-specific global and local alpha coefficients, including the methods tested here (i.e., *STAND* and *Qrev*).

The proposed ANN is a practical tool able to enhance the performances of innovative, non-intrusive, surface velocity-based discharge measurement techniques (e.g., radar- and image-based). The sensitivity analysis of the ANN revealed a significant sensitivity to the shape ratios related to cross-sectional area (R_h and R_{wh}), highlighting the importance of accurately estimating these features for reliable model performance. In contrast, the lower sensitivity to the other input features, particularly for h, suggests that the ANN could be suitable also in scenarios involving satellite-based water depth observations, which are typically subject to higher uncertainty compared to LS-PIV measurements.

The reliability of the proposed ANN was successfully tested in Sicilian rivers with characteristics (e.g., roughness, wetted area, top river width, discharge and average velocity) within the explored ranges during the ANN set-up, defining the model's applicability range. While applicability and suitability in different rivers should be verified, the proposed framework is repeatable and transferable. Moreover, the periodic updating and recalibration of the ANN to accommodate new cases could potentially extend its applicability range.

5. Conclusions

This study investigated the variability of the alpha coefficient, often used for converting surface velocity into depth-averaged velocity for discharge estimation through surface velocity-based methods. A rigorous procedure was implemented to derive empirical vertical velocity profiles from ADCP data collected in various field cases across Sicily, Italy. This procedure allowed for the calculation of the corresponding empirical local alpha values (α_l), and differentiated between profiles that adhere significantly to a power law (PL) and those that do not (NPL). The key findings from the analysis of all empirical α_l values can be summarized as follows:

- the α_l values exhibit significant variability, ranging from 0.62 to 1.50, often deviating from the commonly used standard value of 0.857 (α^*);
- α^* satisfactorily approximates the empirical α_l values only in vertical with PL profiles, which constituted the 30 % of the profiles derived in this study;
- especially for PL cases, α_l increases, and its variability decreases, with water depth (h) at the evaluation point and its distance from the nearest bank (d). Conversely, in verticals with shallower water depths and/or closer to banks, α_l values are generally lower and more variable, indicating potential disturbances from riverbed and riverbank roughness;
- using the generated dataset, an ANN revealed a clear functional relationship ($R^2 = 0.80$) for PL cases between the α_l values along a transect and some easily measurable variables, that are h and d and two shape ratios relative to the cross-sectional area; although this relationship is less clear in NPL cases, the ANN provided for these cases α_l estimations with errors comparable to those from the standard α^*;
- a comparison of practical methods for estimating alpha, applied to four real cases with LS-PIV measurements, showed that the ANN outperformed conventional approaches in terms of reproduction of the distribution of the depth-averaged velocity along measurement transects (i.e., lowest $RMSE_{Vdep}$ for all cases, Table 3). It was the best-performing method for discharge estimation in two cases, providing estimations rather close to those obtained with the standard alpha for the remaining two cases.

This study underscores the importance of local alpha coefficients over a constant global value in improving discharge estimation accuracy. Using simplified approaches, such the ANN here proposed, this is possible also without using expensive and not always usable instrumentations, such the ADCP. Although the analysis covered a wide range of cases, only small rivers with predominantly torrential and, in some cases, ephemeral flow regimes were considered. The roughness conditions examined are those that predominantly characterize Sicilian rivers, and the ADCP measurements were conducted prevalently under ordinary flow conditions. Thus, while the findings align with other studies on different river types, they should be contextualized exclusively to rivers and conditions similar to those explored here. The same considerations should be extended to the suitability of the proposed ANN. Given the growing interest in contactless river monitoring methods, conducting similar analyses on other rives types would be highly beneficial to validate and expand the applicability of these results and the proposed ANN. This represents a promising direction for future research.

CRediT authorship contribution statement

Dario Pumo: Writing – review & editing, Writing – original draft, Visualization, Validation, Supervision, Software, Resources, Methodology, Investigation, Formal analysis, Data curation, Conceptualization. **Francesco Alongi:** Writing – review & editing, Software, Methodology, Investigation, Formal analysis, Data curation. **Carmelo Nasello:** Writing – review & editing, Investigation, Data curation. **Leonardo V. Noto:** Writing – review & editing, Supervision, Resources, Project administration, Investigation, Funding acquisition, Formal analysis.

Declaration of competing interest

The authors declare that they have no known competing financial interests or personal relationships that could have appeared to influence the work reported in this paper.

Acknowledgments

Field campaigns were conducted within the research agreement entitled "*Campagna triennale di misure di portata per l'elaborazione delle scale di deflusso sotto il coordinamento tecnico di ISPRA per supportare il Progetto sul Bilancio Idrologico Nazionale, in corso di realizzazione da parte di ISPRA*" (CUP: F62G16000000001 - Piano Operativo Ambiente FSC 2014-2020 – Asse 2 – Linea di Azione 2.3.1) between the Regional Basin's Authority of Sicily (Autorità di Bacino del Distretto Idrografico della Sicilia) and the Department of Engineering of the University of Palermo. The authors also thank anonymous reviewers for their helpful suggestions on the quality improvement of the present paper.

Funding

This research did not receive any specific grant from funding agencies in the public, commercial, or not-for-profit sectors.

Appendix A. Supplementary data

Supplementary data to this article can be found online at https://doi.org/10.1016/j.jhydrol.2024.132468.

Data availability

Data will be made available on request.

References

Absi, R., 2011. An ordinary differential equation for velocity distribution and dip-phenomenon in open channel flows. J. Hydraul. Res. 49, 82–89. https://doi.org/10.1080/00221686.2010.535700.

Afzalimehr, H., Dey, S., 2009. Influence of bank vegetation and gravel bed on velocity and Reynolds stress distributions. Int. J. Sedim. Res. 24, 236–246. https://doi.org/10.1016/S1001-6279(09)60030-5.

Afzalimehr, H., Maddahi, M.R., Sui, J., Rahimpour, M., 2019. Impacts of vegetation over bedforms on flow characteristics in gravel-bed rivers. J. Hydrodyn. 31, 986–998. https://doi.org/10.1007/s42241-019-0053-x.

Alimenti, F., Bonafoni, S., Gallo, E., Palazzi, V., Vincenti Gatti, R., Mezzanotte, P., Roselli, L., Zito, D., Barbetta, S., Corradini, C., Termini, D., Moramarco, T., 2020. Noncontact measurement of river surface velocity and discharge estimation with a low-cost doppler radar sensor. IEEE Trans. Geosci. Remote Sensing 58, 5195–5207. https://doi.org/10.1109/TGRS.2020.2974185.

Alongi, F., Pumo, D., Nasello, C., Nizza, S., Ciraolo, G., Noto, L.V., 2023. An automatic ANN-based procedure for detecting optimal image sequences supporting LS-PIV applications for rivers monitoring. J. Hydrol. 626, 130233. https://doi.org/10.1016/j.jhydrol.2023.130233.

Arnell, N.W., Gosling, S.N., 2013. The impacts of climate change on river flow regimes at the global scale. J. Hydrol. 486, 351–364. https://doi.org/10.1016/j.jhydrol.2013.02.010.

Bahmanpouri, F., Barbetta, S., Gualtieri, C., Ianniruberto, M., Filizola, N., Termini, D., Moramarco, T., 2022a. Prediction of river discharges at confluences based on Entropy theory and surface-velocity measurements. J. Hydrol. 606, 127404. https://doi.org/10.1016/j.jhydrol.2021.127404.

Bahmanpouri, F., Eltner, A., Barbetta, S., Bertalan, L., Moramarco, T., 2022b. Estimating the average river cross-section velocity by observing only one surface velocity value and calibrating the entropic parameter. Water Resour. Res. 58, e2021WR031821. https://doi.org/10.1029/2021WR031821.

Biggs, H., Smart, G., Holwerda, N., Doyle, M., McDonald, M., Ede, M., 2021. River discharge from surface velocity measurements: A field guide for selecting alpha. https://doi.org/10.13140/RG.2.2.22159.05282/1.

Biggs, H., Smart, G., Doyle, M., Eickelberg, N., Aberle, J., Randall, M., Detert, M., 2023. Surface velocity to depth-averaged velocity—a review of methods to estimate alpha and remaining challenges. Water 15, 3711. https://doi.org/10.3390/w15213711.

Bonakdari, H., Larrarte, F., Lassabatere, L., Joannis, C., 2008. Turbulent velocity profile in fully-developed open channel flows. Environ. Fluid Mech. 8, 1–17. https://doi.org/10.1007/s10652-007-9051-6.

Bradbrook, K.F., Lane, S.N., Richards, K.S., 2000. Numerical simulation of three-dimensional, time-averaged flow structure at river channel confluences. Water Resour. Res. 36, 2731–2746. https://doi.org/10.1029/2000WR900011.

Chen, F.-W., Liu, C.-W., 2020. Assessing the applicability of flow measurement by using non-contact observation methods in open channels. Environ Monit Assess 192, 289. https://doi.org/10.1007/s10661-020-8226-1.

Chiu, C.L., 1989. Velocity distribution in open channel flow. J. Hydraul. Eng. 115, 576–594. https://doi.org/10.1061/(ASCE)0733-9429(1989)115:5(576).

Costa, J.E., Spicer, K.R., Cheng, R.T., Haeni, F.P., Melcher, N.B., Thurman, E.M., Plant, W.J., Keller, W.C., 2000. measuring stream discharge by non-contact methods: a proof-of-concept experiment. Geophys. Res. Lett. 27, 553–556. https://doi.org/10.1029/1999GL006087.

Costa, J.E., Cheng, R.T., Haeni, F.P., Melcher, N., Spicer, K.R., Hayes, E., Plant, W., Hayes, K., Teague, C., Barrick, D., 2006. Use of radars to monitor stream discharge by noncontact methods: NONCONTACT STREAMFLOW. Water Resour. Res. 42. https://doi.org/10.1029/2005WR004430.

Creutin, J.D., Muste, M., Bradley, A.A., Kim, S.C., Kruger, A., 2003. River gauging using PIV techniques: a proof of concept experiment on the Iowa River. J. Hydrol. 277, 182–194. https://doi.org/10.1016/S0022-1694(03)00081-7.

Dal Sasso, S.F., Pizarro, A., Samela, C., Mita, L., Manfreda, S., 2018. Exploring the optimal experimental setup for surface flow velocity measurements using PTV. Environ. Monit. Assess. 190, 460. https://doi.org/10.1007/s10661-018-6848-3.

Despax, A., Perret, C., Garçon, R., Hauet, A., Belleville, A., Le Coz, J., Favre, A.-C., 2016. Considering sampling strategy and cross-section complexity for estimating the uncertainty of discharge measurements using the velocity-area method. J. Hydrol. 533, 128–140. https://doi.org/10.1016/j.jhydrol.2015.11.048.

Díaz Lozada, J.M., Garcia, C.M., Oberg, K., Over, T.M., Nieto, F.F., 2023. Improvements to estimate ADCP uncertainty sources for discharge measurements. Flow Meas. Instrum. 90, 102311. https://doi.org/10.1016/j.flowmeasinst.2023.102311.

Farnebäck, G., 2003. Two-Frame Motion Estimation Based on Polynomial Expansion, in: Bigun, J., Gustavsson, T. (Eds.), Image Analysis, Lecture Notes in Computer Science. Springer Berlin Heidelberg, Berlin, Heidelberg, pp. 363–370. https://doi.org/10.1007/3-540-45103-X_50.

Francis, J.B., 1878. On the cause of the maximum velocity of water flowing in open channels being below the surface. T. Am. Soc. Civ. Eng. 7, 109–113. https://doi.org/10.1061/TACEAT.0000315.

Fujita, I., Muste, M., Kruger, A., 1998. Large-scale particle image velocimetry for flow analysis in hydraulic engineering applications. J. Hydraul. Res. 36, 397–414. https://doi.org/10.1080/00221689809498626.

Fulton, J.W., Mason, C., Eggleston, J., Nicotra, M., Chiu, C.L., et al., 2020. Remote sensing of surface velocity and river discharge using radars and the probability concept at 10 USGS stream gages. Remote Sens. 12 (8), 1296. https://doi.org/10.3390/rs12081296.

Fulton, J., Ostrowski, J., 2008. Measuring real-time streamflow using emerging technologies: Radar, hydroacoustics, and the probability concept. J. Hydrol. 357, 1–10. https://doi.org/10.1016/j.jhydrol.2008.03.028.

Guo, J., Julien, P.Y., Meroney, R.N., 2005. Modified log-wake law for zero-pressure-gradient turbulent boundary layers. J. Hydraul. Res. 43, 421–430. https://doi.org/10.1080/00221680509500138.

Harding, S.F., Coleman, A.M., Roegner, G.C., 2020. Comparison of experimental and computational methods for discharge measurements from tidal wetlands. River Res. Apps 36, 1954–1961. https://doi.org/10.1002/rra.3709.

Hauet, A., Kruger, A., Krajewski, W.F., Bradley, A., Muste, M., Creutin, J.-D., Wilson, M., 2008. Experimental System for Real-Time Discharge Estimation Using an Image-Based Method. J. Hydrol. Eng. 13, 105–110. https://doi.org/10.1061/(ASCE)1084-0699(2008)13:2(105).

Hauet, A., Morlot, T., Daubagnan, L., 2018. Velocity profile and depth-averaged to surface velocity in natural streams: a review over a large sample of rivers. E3S Web Conf. 40, 06015. https://doi.org/10.1051/e3sconf/20184006015.

Herschy, R.W., 1998. Velocity-area method. In: Encyclopedia of Hydrology and Lakes, Encyclopedia of Earth Science. Springer, Netherlands, pp. 668–670. https://doi.org/10.1007/1-4020-4497-6_228.

Huai, W., Zhang, J., Katul, G.G., Cheng, Y., Tang, X., Wang, W., 2019. The structure of turbulent flow through submerged flexible vegetation. J Hydrodyn 31, 274–292. https://doi.org/10.1007/s42241-019-0023-3.

ISO 748:2021. Hydrometry — Measurement of liquid flow in open channels — Velocity area methods using point velocity measurements. (Edition 5, 2021, Publication date: 2021-11). P.42. International Standard. Technical Committee: ISO/TC 113/SC 1. ICS: 17.120.20.

Johnson, E.D., Cowen, E.A., 2017. Remote determination of the velocity index and mean streamwise velocity profiles. Water Resour. Res. 53, 7521–7535. https://doi.org/10.1002/2017WR020504.

Kim, Y., Muste, M., Hauet, A., Krajewski, W.F., Kruger, A., Bradley, A., 2008. Stream discharge using mobile large-scale particle image velocimetry: a proof of concept. Water Resour. Res. 44, 2006WR005441. https://doi.org/10.1029/2006WR005441.

Koussis, A.D., Dimitriadis, P., Lykoudis, S., Kappos, N., Katsanos, D., Koletsis, I., Psiloglou, B., Rozos, E., Mazi, K., 2022. Discharge estimation from surface-velocity observations by a maximum-entropy based method. Hydrol. Sci. J. 67 (3), 451–461. https://doi.org/10.1080/02626667.2022.2030059.

Kundu, S., Ghoshal, K., 2012. An analytical model for velocity distribution and dip-phenomenon in uniform open channel flows. InterJFluidMechRes 39, 381–395. https://doi.org/10.1615/InterJFluidMechRes.v39.i5.20.

Lassabatere, L., Pu, J.H., Bonakdari, H., Joannis, C., Larrarte, F., 2013. Velocity distribution in open channel flows: analytical approach for the outer region. J. Hydraul. Eng. 139, 37–43. https://doi.org/10.1061/(ASCE)HY.1943-7900.0000609.

Le Coz, J., Pierrefeu, G., Paquier, A., 2008. Evaluation of river discharges monitored by a fixed side-looking Doppler profiler: evaluation of river discharges monitored by a H-ADCP. Water Resour. Res. 44. https://doi.org/10.1029/2008WR006967.

Le Coz, J., Hauet, A., Pierrefeu, G., Dramais, G., Camenen, B., 2010. Performance of image-based velocimetry (LSPIV) applied to flash-flood discharge measurements in Mediterranean rivers. J. Hydrol. 394, 42–52. https://doi.org/10.1016/j.jhydrol.2010.05.049.

Le Coz, J., Camenen, B., Peyrard, X., Dramais, G., 2012. Uncertainty in open-channel discharges measured with the velocity–area method. Flow Meas. Instrum. 26, 18–29. https://doi.org/10.1016/j.flowmeasinst.2012.05.001.

Le Coz, J., Jodeau, M., Hauet, A., Marchand, B., Le Boursicaud, R., 2014. Image-based velocity and discharge measurements in field and laboratory river engineering studies using the free FUDAA-LSPIV software, in: Proceedings of the International Conference on Fluvial Hydraulics, River Flow. pp. 2014–05.

Lee, J.S., Julien, P.Y., 2006. Electromagnetic wave surface velocimetry. J. Hydraul. Eng. 132 (2), 146–153. https://doi.org/10.1061/(ASCE)0733-9429(2006)132:2(146).

Lee, H.-E., Lee, C., Kim, Y.-J., Kim, J.-S., Kim, W., 2013. Power law exponents for vertical velocity distributions in natural rivers. ENG 05, 933–942. https://doi.org/10.4236/eng.2013.512114.

Legleiter, C.J., Kinzel, P.J., 2021. Surface flow velocities from space: particle image velocimetry of satellite video of a large. Sedim.-Laden River. Front. Water 3, 652213. https://doi.org/10.3389/frwa.2021.652213.

Li, D., Zhong, Q., Yu, M., Wang, X., 2013. Large-scale particle tracking velocimetry with multi-channel CCD cameras. Int. J. Sedim. Res. 28, 103–110. https://doi.org/10.1016/S1001-6279(13)60022-0.

Ljubičić, R., Dal Sasso, S.F., Zindović, B., 2024. SSIMS-flow: image velocimetry workbench for open-channel flow rate estimation. Environ. Model. Softw. 173, 105938. https://doi.org/10.1016/j.envsoft.2023.105938.

Moramarco, T., Barbetta, S., Tarpanelli, A., 2017. From surface flow velocity measurements to discharge assessment by the entropy theory. Water 9, 120. https://doi.org/10.3390/w9020120.

Moramarco, T., Singh, V.P., 2010. Formulation of the entropy parameter based on hydraulic and geometric characteristics of river cross sections. J. Hydrol. Eng. 15, 852–858. https://doi.org/10.1061/(ASCE)HE.1943-5584.0000255.

Mueller, D.S., 2016. QRev—Software for computation and quality assurance of acoustic doppler current profiler moving-boat streamflow measurements—technical manual for version 2.8 (Open-File Report), Open-File. Report.

Mueller, D.S., Wagner, C.R., Rehmel, M.S., Oberg, K.A., Rainville, F., 2009. Measuring discharge with acoustic Doppler current profilers from a moving boat. US Department of the Interior, US Geological Survey Reston, Virginia (EUA).

Muste, M., Fujita, I., Hauet, A., 2008. Large-scale particle image velocimetry for measurements in riverine environments: large-scale particle velocimetry. Water Resour. Res. 44. https://doi.org/10.1029/2008WR006950.

Papadimitrakis, I.A., Orphanos, I., 2009. Statistical analysis of river characteristics (in Greece): basic hydraulic parameters. Hydrol. Sci. J. 54, 1035–1052. https://doi.org/10.1623/hysj.54.6.1035.

Patalano, A., García, C.M., Rodríguez, A., 2017. Rectification of Image Velocity Results (RIVeR): a simple and user-friendly toolbox for large scale water surface Particle Image Velocimetry (PIV) and Particle Tracking Velocimetry (PTV). Comput. Geosci. 109, 323–330. https://doi.org/10.1016/j.cageo.2017.07.009.

Pelletier, P.M., 1988. Uncertainties in the single determination of river discharge: a literature review. Can. J. Civ. Eng. 15, 834–850. https://doi.org/10.1139/l88-109.

Perks, M.T., 2020. KLT-IV v1.0: image velocimetry software for use with fixed and mobile platforms. Geosci. Model Dev. 13, 6111–6130. https://doi.org/10.5194/gmd-13-6111-2020.

Petrie, J., Diplas, P., 2016. Evaluation of the logarithmic law of the wall for river flows. River Res. Apps 32, 1082–1093. https://doi.org/10.1002/rra.2920.

Pumo D., Noto L.V. Exploring the use of multi-gene genetic programming in regional models for the simulation of monthly river runoff series (2023), Stochastic Environmental Research and Risk Assessment, DOI: 10.1007/s00477-022-02373-1.

Pumo D., Alongi F., Ciraolo G., Noto L.V. Optical methods for river monitoring: A simulation-based approach to explore optimal experimental setup for LSPIV (2021), Water, 13 (3), Article number 247 (27p), DOI: 10.3390/w13030247.

Rantz, S.E., 1982. Measurement and computation of streamflow. US Department of the Interior, Geological Survey.

Sarma, K.V.N., Prasad, B.V.R., Sarma, A.K., 2000. Detailed Study of Binary Law for Open Channels. J. Hydraul. Eng. 126, 210–214. https://doi.org/10.1061/(ASCE)0733-9429(2000)126:3(210).

Smart, G.M., Biggs, H.J., 2020. Remote gauging of open channel flow: Estimation of depth averaged velocity from surface velocity and turbulence, in: Uijttewaal, W., J. Franca, M., Valero, D., Chavarrias, V., Ylla Arbós, C., Schielen, R., Crosato, A. (Eds.), River Flow 2020. CRC Press, pp. 1035–1044. https://doi.org/10.1201/b22619-145.

Tauro, F., Piscopia, R., Grimaldi, S., 2017. Streamflow Observations From Cameras: Large-Scale Particle Image Velocimetry or Particle Tracking Velocimetry? Water Resour. Res. 53, 10374–10394. https://doi.org/10.1002/2017WR020848.

Thielicke, W., Stamhuis, E.J., 2014. PIVlab – towards user-friendly, affordable and accurate digital particle image velocimetry in MATLAB. J. Open Res. Softw. 2. https://doi.org/10.5334/jors.bl.

Turnipseed, D.P., Sauer, V.B., 2010. Discharge measurements at Gaging stations. U.S. Geological Survey, Techniques and Methods, book 3, chap. A8, 87 p. (Also available at http://pubs.usgs.gov/tm/tm3-a8/.) https://doi.org/10.3133/tm3A8.

Vyas, J.K., Perumal, M., Moramarco, T., 2020. Discharge estimation using tsallis and shannon entropy theory in natural channels. Water 12, 1786.

Vyas, J.K., Perumal, M., Moramarco, T., 2024. Non-contact discharge estimation at a river site using only the maximum surface flow velocity. J. Hydrol. 638, 131505. https://doi.org/10.1016/j.jhydrol.2024.131505.

Welber, M., Le Coz, J., Laronne, J.B., Zolezzi, G., Zamler, D., Dramais, G., Hauet, A., Salvaro, M., 2016. Field assessment of noncontact stream gauging using portable surface velocity radars (SVR). Water Resour. Res. 52, 1108–1126. https://doi.org/10.1002/2015WR017906.

Willmott, C.J., Robeson, S.M., Matsuura, K., 2012. A refined index of model performance. Int. J. Climatol. 32, 2088–2094. https://doi.org/10.1002/joc.2419.

WMO, 2008. World Meteorological Organization (Ed.), 2008. Guide to hydrological practices, 6th ed. ed, WMO. WMO, Geneva, Switzerland.

Yang, S.-Q., Tan, S.-K., Lim, S.-Y., 2004. Velocity distribution and dip-phenomenon in smooth uniform open channel flows. J. Hydraul. Eng. 130, 1179–1186. https://doi.org/10.1061/(ASCE)0733-9429(2004)130:12(1179).